Stratocumulus Cloud Properties Derived from Simultaneous Satellite and Island-based Instrumentation during FIRE

PATRICK MINNIS

Atmospheric Sciences Division, NASA Langley Research Center, Hampton, Virginia

PATRICK W. HECK AND DAVID F. YOUNG

Lockheed Engineering and Sciences Company, Hampton, Virginia

C. W. FAIRALL AND J. B. SNIDER

NOAA Wave Propagation Laboratory, Boulder, Colorado

(Manuscript received 1 June 1991, in final form 18 September 1991)

ABSTRACT

Cloud parameters derived from visible and infrared window data from the Geostationary Operational Environmental Satellite (GOES) are compared to corresponding properties determined from instrumentation on San Nicolas Island off the coast of California during the First ISCCP Regional Experiment (FIRE) marine stratocumulus intensive field observations period in July 1987. Mean cloud amounts derived by applying the hybrid bispectral threshold method to the GOES data were 5% less than the island ceilometer measurements. Examination of the satellite imagery revealed that the apparent bias can be explained by the persistence of the clouds over the northwest part of the island during periods of clearing around the island. Diurnal variations in the cloud cover were very significant; minimum cloudiness occurred during the late afternoon and maximum cloudiness early in the morning. The satellite retrievals track this variation quite well. Satellite-derived mean cloud-top height is 53 m lower than that observed from the surface. Relationships were established between the satellite-derived cloud optical depth and two surface-observed quantities: cloud liquid water path and cloud thickness. Simultaneous observations of liquid water path and satellite-derived cloud optical depth were used to infer effective cloud-droplet radius, resulting in good agreement with correlative data. The diurnal variations in cloud amount are accompanied by changes in cloud thickness, cloud-top height, cloud liquid water path, and effective droplet size. These observations provide the most complete picture, to date, of the diurnal cycle of marine stratocumulus clouds, confirming previous satellite-based inferences of the diurnal behavior of marine stratocumulus at larger scales. Because of the limited area of the observations, further comparisons should be performed over other regions containing climatologically significant marine stratocumulus clouds.

1. Introduction

Radiance measurements taken by operational meteorological satellites provide the only means for routine global monitoring of many atmospheric quantities needed for weather and climate prediction. Interpretations of these radiances to derive values for such variables as cloud amount or liquid water are highly uncertain because of the variable nature of clouds and the difficulties associated with establishing cloud truth. The need for validating, improving, and expanding these interpretations, however, has become acute since the onset of the International Satellite Cloud Climatology Project (ISCCP; see Schiffer and Rossow 1983). In the coming years, results from satellite data analyses such as the ISCCP will be the major source for statistics of global cloud properties. Climate modeling efforts that attempt to account for cloud cover will most likely use these results as references for evaluating model capabilities. For such efforts, knowledge of the limitations of the satellite-derived products is essential.

The First ISCCP Regional Experiment (FIRE; see Starr 1987) provides a unique opportunity to assess satellite retrievals of cloud parameters because of the availability of simultaneous monitoring of various cloud properties from the ground and from aircraft. Comprehensive, detailed cloud measurements taken off the coast of California during the FIRE marine stratocumulus intensive field observation (IFO) period (Albrecht et al. 1988), 29 June–19 July 1987, constitute a dataset useful for examining retrievals over one type of cloud system. This study uses some of the IFO data to evaluate the cloud properties derived from Geostationary Operational Environmental Satellite (GOES)

Corresponding author address: Dr. Patrick Minnis, NASA Langley Research Center, Mail Stop 420, 21 Ames Rd, Hampton, VA 23665-5225.

data taken in the vicinity of San Nicolas Island (SNI). The hybrid bispectral threshold method, HBTM, described by Minnis et al. (1987), is applied here to GOES data on a small-scale grid surrounding the island. The satellite retrievals are then compared with the SNI surface-based data, which can be regarded as a ground-truth set. The uncertainties derived from the comparison represent a calibration of the HBTM. Results from this same methodology applied to a larger-scale dataset containing similar cloud fields can then be used to evaluate cloud products derived with other methods, such as that used by ISCCP, from data taken over the same cloud fields.

This paper presents the results of the first step in that process, comparing the small-scale analyses with surface observations. These comparisons can lead to methodology enhancements and new insights into the properties of stratocumulus clouds in addition to the validation of current technologies.

2. Data and methodology

a. Surface data

The surface site was on the northwestern point of the island, which is situated southwest of Los Angeles at 33.29°N, 119.56°W (Fig. 1). Prevailing winds are northwesterly, so advection over the site was usually onshore. A ceilometer, an acoustic sounder, broadband shortwave and longwave flux radiometers, a three-channel microwave radiometer, and conventional meteorological instruments were used to derive cloud fraction, cloud-base height, inversion base (or cloud-top) altitude, cloud albedo, and cloud liquid water path. Details of the instruments and analyses are given by Hogg et al. (1983), Albrecht et al. (1988), and Fairall et al. (1990).

All single-valued (from only one instrument), surface-derived parameters in this paper are denoted with the subscript s. Other parameters having values that were derived from two different surface instruments are subscripted with the initial of the respective instrument. Corresponding satellite-derived variables have no subscripts, but satellite-derived temperatures do have subscripts because no corresponding surface-based values are used. The 30-s ceilometer data were averaged to obtain hourly means of cloud-base height z_s^b and cloud fraction C_c centered at 10 min before the UTC (universal time coordinated) hour. The ceilometer cloud fraction is the number of measurements containing a cloud divided by the total number of measurements directly over the site. The ceilometer returns an instantaneous point measurement that, when averaged over time, corresponds to a line measurement along the wind direction. Continuous acoustic sounder measurements were averaged in the same manner to produce cloud-top height z_s^t using the assumption that the base of the inversion corresponds to the cloud top. Mean hourly cloud thickness, $\Delta z_s = z_s^t - z_s^b$, was derived from the ceilometer and acoustic sounder data. Cloud fraction was also estimated with the longwave radiometer data and designated as C_r. The longwave cloud-fraction analysis attempts to account for the fractional cloudiness within the field of view of the radiometer. Assuming the effective radiation comes from within 75° of the zenith, the effective field of view is ~11 km^2 for a cloud base at 0.5 km. Thus, C_r corresponds to an instantaneous areal measurement that becomes a strip when averaged over time.

The integrated liquid water path (LWP) is computed from the transmitted shortwave flux measurements (Fairall et al. 1990) using a modified version of the parameterization of Stephens (1978) to produce W_r, the radiometer LWP. The microwave instrument was also used to monitor a liquid water path continuously over all hours of the day. One-minute averages were further averaged to obtain hourly values of the micro-

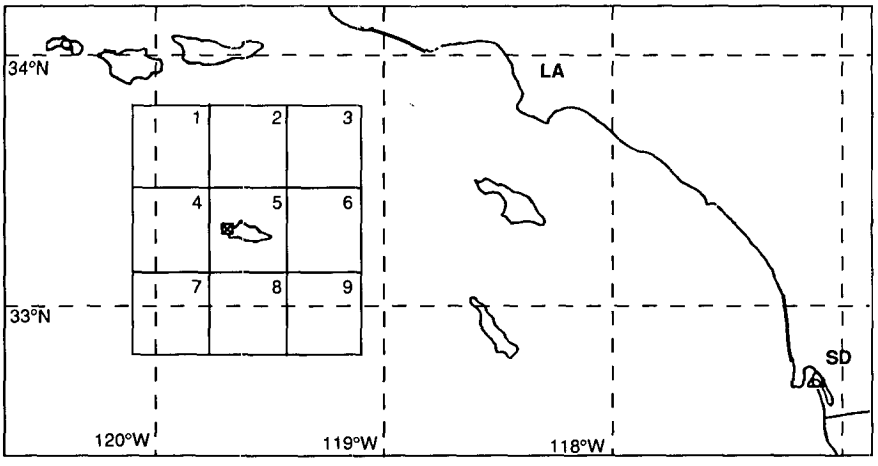

FIG. 1. Analysis grid centered on the San Nicolas Island site off the California coast. The designations LA and SD denote locations of Los Angeles and San Diego, respectively.

wave liquid water path W_m. The LWP data are discussed in detail by Fairall et al. (1990).

b. Satellite data

Hourly *GOES-6* visible (VIS, 0.65-μm) and infrared (IR, 11.5-μm) radiances taken at nominal resolutions of 3.5 km and 3.5 km × 7 km, respectively, were analyzed on a 0.33° latitude–longitude grid centered over the SNI site. The IR resolution was artificially enhanced to 3.5 km by repeating each scan line. Because of an unforeseen spacecraft wobble, a 90-km shift to the nominal navigation was required. Even with the correction, the precision for *GOES-6* was only ±12 km for this time period. Each grid box (Fig. 1) represents an area of roughly 1100 km^2. This box size was selected to minimize the effects of the navigation uncertainty. The box is equivalent to the area represented by one ISCCP pixel, and the number of 3.5-km pixels in the box is more than sufficient for reliable application of the analysis technique. All satellite data were measured approximately 10 min before the UTC hour. Figure 1 shows the location of nine grid boxes and their associated region numbers. *GOES-6* was located over the equator at 135°W so that the grid was viewed at a satellite zenith angle of ~35°. Because almost all of the observed cloudiness was low clouds, total and low cloudiness are used synonymously hereafter. Total cloud fraction and low cloud amount C were derived with the HBTM described by Minnis et al. (1987).

Cloud temperature T'_{cld} from the HBTM is uncorrected for attenuation by the atmosphere above the cloud. To account for the atmosphere, the cloud and clear-sky temperatures were corrected with a modified version of the method of Rossow et al. (1988). Gridded NMC (National Meteorological Center) analyses were used for temperature and humidity at standard levels up to 300 mb. Mean Electra aircraft soundings for the IFO (Albrecht et al. 1988) were used to improve the NMC relative humidity values at 850 mb and surface (1016 mb). The mean Electra soundings are compared with averages of the corresponding NMC analyses in Fig. 2. These comparisons show that the lower troposphere is drier than expected from the NMC analyses. The boundary-layer inversion, absent in the NMC analyses, is quite evident in the Electra data. The corrected cloud-top temperature T_{cld} is usually no more than 0.5 K greater than T'_{cld}. Correction of the clear-sky temperature T'_{sfc} produced a mean surface temperature of T_{sfc} = 16.0°C. Cloud-top altitude in kilometers is

$$z^t = (T_{sfc} - T_{cld})/7.1 \text{ K km}^{-1}.$$

This formula is based on the average boundary-layer lapse rate of 7.1 K km^{-1} derived from the Electra soundings.

The GOES cloud optical depth is $\tau = \tau(\rho, \theta_0, \theta, \psi)$, where ρ is the measured reflectance of the earth–atmosphere system, θ_0 is the solar zenith angle, θ is the satellite zenith angle, and ψ is the relative azimuth angle. The reflectance is computed from the 6-bit GOES visible counts D using the calibration,

$$\rho = (0.16D^2 - 8)/526.9\delta_0\mu_0,$$

reported by Whitlock (1989, personal communication), where δ_0 is the earth–sun distance correction factor and $\mu_0 = \cos\theta_0$. The function τ was determined from the results of adding–doubling radiative transfer calculations using a three-layer model over an ocean

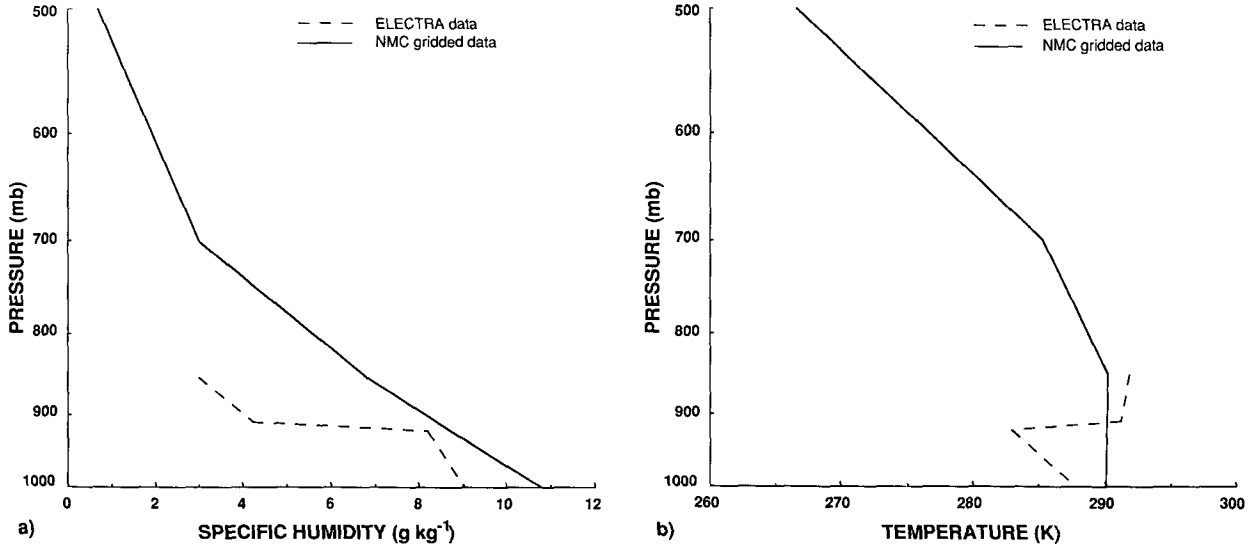

FIG. 2. Comparison of mean soundings of (a) specific humidity and (b) temperature from Electra aircraft and NMC gridded analyses for the 2.5° region containing San Nicolas Island, 30 June–19 July 1987.

surface. The surface albedo in the radiative transfer model is

$$\alpha_{sfc} = 2.8(\mu_0^{1.5} + 0.065) + 15(\mu_0 - 0.1) + (\mu_0 - 0.5)(\mu_0 - 1),$$

which is a variation on the parameterization of Briegleb et al. (1986). The lowest layer in the model is a pure Rayleigh-scattering layer having an optical depth corresponding to a thickness of 75 mb. The second layer is a plane-parallel cloud of varying optical depth, and the cloud optical properties are determined from Mie calculations using the program developed by Wiscombe (1980) for water droplets having a modified gamma size distribution defined by an effective radius of 8 μm and variance of 0.05. The top layer combines the Rayleigh-scattering optical depth corresponding to a 925-mb thickness with the ozone absorption optical depth corresponding to an ozone concentration of 0.32 cm atm. No aerosols are included in the calculations.

Examples of the results of these computations for $\theta_0 = 60°$ are shown in Fig. 3 as anisotropic factors, which are defined as $\chi = \rho(\tau, \theta_0, \theta, \psi)/\alpha(\tau, \theta_0)$, where α is the earth–atmosphere system albedo. This quantity is displayed in order to better contrast the reflectance patterns. Both cases (Figs. 3a and 3b) show strong forward scattering and a minimum of reflectance to the sides and around the zenith. The rainbow feature of the droplet scattering is manifest in the relative maxima around $\theta > 45°$, $\psi = 145°$. This feature is much less prominent for $\tau = 8$ because of increased multiple scattering. Overall, the results in Fig. 3 demonstrate a significant dependence of χ on cloud optical depth. A set of eight lookup tables of $\rho(\tau, \theta_0, \theta, \psi)$ was created for $\tau = 0.25$, 0.5, 1, 2, 4, 8, 16, and 64. The value of τ for a given measured reflectance is determined by linear interpolation on those tables.

Based on Mie-scattering calculations, the cloud emissivity at 11.5 μm is approximated as

$$\epsilon = 1 - \exp(-\tau/2.50).$$

The observed value of T_{cld} may be further corrected using the assumption that $B(T) = (1 - \epsilon)B(T'_{sfc}) + \epsilon B(T'_{cld})$, where B refers to the Planck function at 11.5 μm. This correction can be applied only during the daytime. Unless otherwise noted, all values of T_{cld} are not corrected for emissivity.

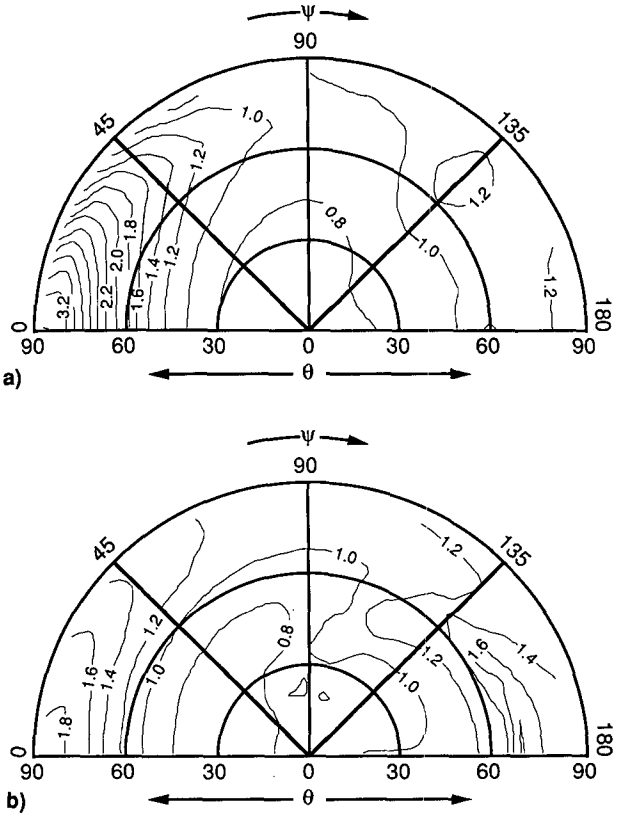

FIG. 3. Examples of anisotropic reflectance factors for cloud over ocean based on radiative transfer calculations using $r = 8$ μm; (a) $\tau = 8$, $\theta_0 = 60°$, (b) $\tau = 2$, $\theta_0 = 60°$.

3. Results

a. Satellite results over greater SNI regions

The averaged satellite cloud parameters provide an overview of the cloud conditions around SNI. Figure 4 shows a plot of the mean HBTM-derived cloud fraction for the greater IFO area (Young et al. 1990), which extends from 28° to 38°N and 126° to 116°W. The inset in Fig. 4 delineates the cloudiness over the SNI grid (Fig. 1). The mean grid cloud fraction was 68% for the 21-day period. Mean cloudiness ranged from ~55% over the regions north of SNI to ~78% south of the island. The mean cloud optical depth was 11.1; it varied from 10.2 in regions 1 and 2 to 12.0 in region 9. These quantities also exhibited significant diurnal variability, as shown in Fig. 5. Mean cloudiness for the study area ranged from 89% near 0600 LST (local solar time) to 44% around 1700 LST. The cloud optical depth appears to peak at 16.1 around 1000 LST, dropping to ~3.0 near sunset. These variations suggest that the clouds continue to gain water even as they begin to break up in the morning. The optical depth decreases almost linearly with the rapid dissipation of the clouds after 1000 LST.

Clear-sky temperature varied from 288.9 K northwest of SNI to 287.4 K in region 7. East of the island, $T'_{sfc} = 288.8$ K. These results are consistent with aircraft observations (Jensen 1990), which indicate that the sea surface temperature increased upwind (northwest) of SNI. Corrections for atmospheric attenuation produced $T_{sfc} = 289.5$ K averaged over all the regions. The mean uncorrected average cloud-top temperature T'_{cld} was 284.5 K for all of the regions. It varied by only 1 K from 283.8 K in region 7 to 284.8 K in regions

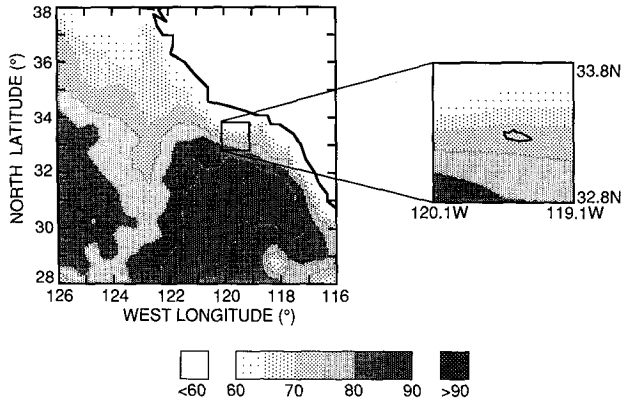

FIG. 4. Mean cloud amounts in percent from hybrid bispectral threshold method analysis of GOES data over IFO (large box) and SNI (inset) areas, 30 June–19 July 1987.

1–3. Atmospheric corrections yield T_{cld} = 284.1 K. The temperatures also varied with time of day, as seen in Fig. 6. Temperature T'_{sfc} changed by 1 K from a minimum near 0700 LST to a broad maximum during the afternoon, while T'_{cld} increased by 2 K from 0700 LST to the late afternoon, suggesting a lowering of the cloud tops as they dissipated. Although the diurnal trends in Figs. 5 and 6 are fairly representative of the regions in the grid, there are some interregional differences as might be expected from the gradients in C, τ, and T'_{sfc}. These differences are discussed in section 3c.

b. Contemporaneous comparisons

Figures 7a and 7b present a comparison of the daytime values of C for region 5 with the corresponding contemporaneous values of C_c and C_r, respectively.

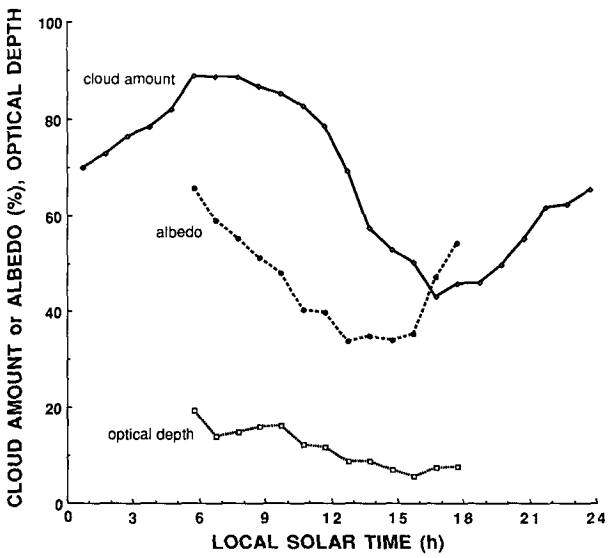

FIG. 5. Mean cloud properties for the nine regions in the SNI grid (Fig. 1), 30 June–19 July 1987.

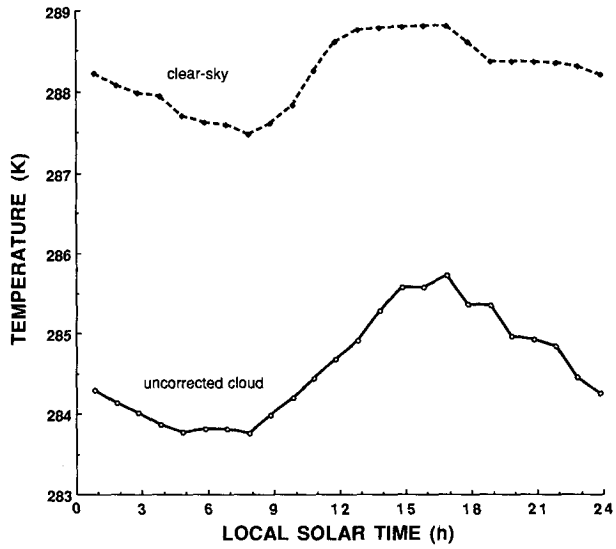

FIG. 6. Mean clear-sky and uncorrected cloud temperatures from HBTM analysis of GOES data for the nine regions in the SNI grid, 30 June–19 July 1987.

The satellite analysis generally retrieves less cloudiness than that derived from the ceilometer data. In both cases there is considerable scatter in the data despite the correlation coefficients, R = 0.84 for C_c and 0.89 for C_r. The slightly greater scatter in Fig. 7a, equivalent to an rms difference of 17% compared to 15% for Fig. 7b, probably reflects the disparity in spatial scale between the two surface instruments. Some dispersion between the surface and satellite data is expected for the same reason. The ceilometer frequently obtains totally clear and overcast conditions, whereas the radiometer algorithm retrieves a few overcast and virtually no clear skies. The radiometer algorithm is tied to a predetermined clear-sky and overcast flux. Apparently, the longwave fluxes for clear skies and overcast conditions during the IFO were different from those of the predetermined algorithm values. Discrepancies between the two surface cloud amounts are more apparent in a direct comparison of their respective daytime data in Fig. 8. The scatter in these data, which corresponds to an rms difference of 13%, may be the result of differences between the algorithms or between the clouds directly over the site and those over the surrounding water.

If the satellite retrievals were always correct, there would be no values of C = 0 or 100% when $C_c > 0$ or $C_c < 100\%$, respectively, assuming the ceilometer always detects clouds and cloud holes. The ceilometer, however, determines cloud fraction from a time series of binary data. The satellite takes an instantaneous picture, so clouds present in the area during the previous half hour and observed by the ceilometer may have dissipated. During the half hour after the image time, some clouds may have developed over the surface

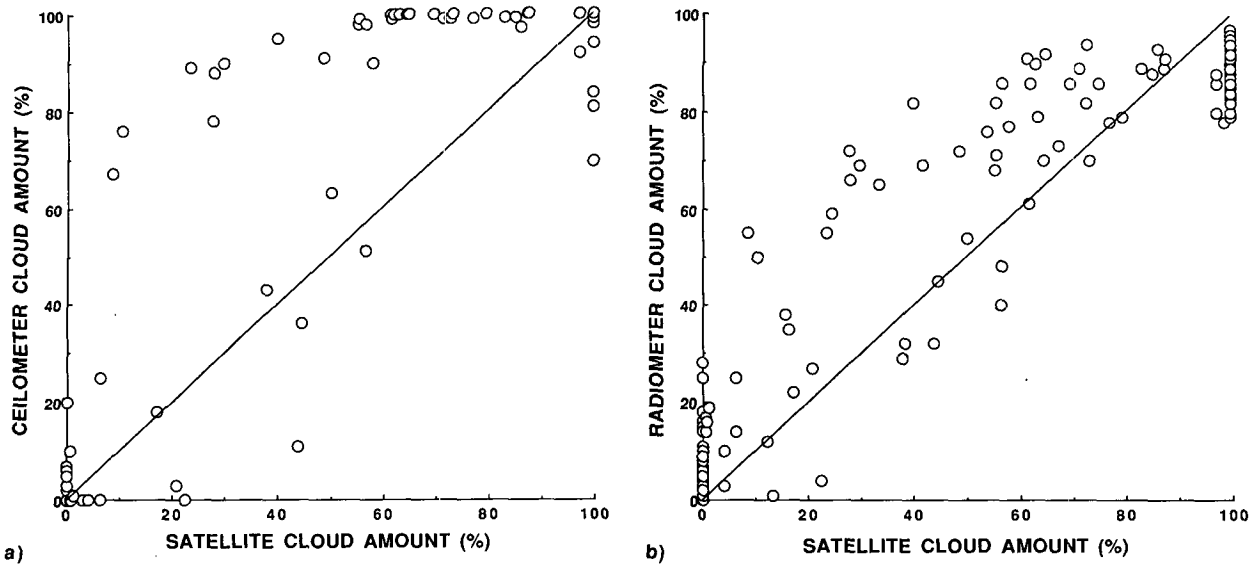

FIG. 7. Comparison of hourly daytime, region 5 HBTM (satellite) and surface-based (a) ceilometer and (b) radiometer cloud amounts, 30 June–19 July 1987.

site. Similarly, holes could have formed and closed between the image times. This problem of temporal versus spatial averaging is always a potential source of difference between the satellite and the surface observations whenever the region is either completely clear or overcast or covered by a constant, homogeneous cloud field for the entire hour surrounding the satellite image time. Although the differences arising from this source cannot be completely reconciled here, they are explored in more detail in section 4a.

There were a few instances, however, when the algorithm failed to detect some small amounts of cloudiness that were observed with the ceilometer. The VIS–IR histograms (used in the HBTM) corresponding to some of these cases were scrutinized to better understand the discrepancies. For several cases with $C = 0$, $C_c > 0$, the presence of clouds is indicated by a range in the VIS data that is slightly greater than that expected for a clear scene. None of the apparent cloudy pixels, however, are bright enough to exceed the lowest cloud threshold in the HBTM. In several other cases, there are some brighter pixels that were directly over the island so that their temperatures were a few degrees greater than T'_{sfc}. For regions containing some, but less than 5%, land (region 5, for example), the HBTM allows a few pixels that are brighter and warmer to be classified as clear pixels. Thus, the brighter warmer pixels were classified as clear. Several histograms for $C = 100\%$ and $C_c < 100\%$ were also examined. The histograms are typically very bright, with some variation in reflectance but not in temperature. Perhaps the cloud decks were composed of regular arrays of very bright cells with some spacing so that no pixels were dim enough to be classified as clear or partly cloudy by the HBTM or the holes in the deck were not present at the image time.

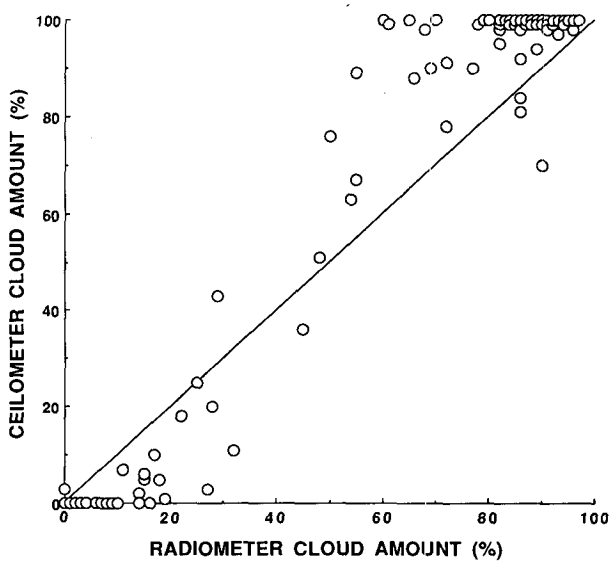

FIG. 8. Comparison of hourly daytime, surface-based cloud amounts, 1–19 July 1987.

At night, the correlation coefficient between C and C_c is reduced to 0.61. None of the cases with $C = 0$, $C_c \neq 0$, however, occur at night. The linear regression fit is nearly identical to the daytime results, indicating good consistency in the HBTM between the bispectral daytime and unispectral nighttime algorithms. The rms instantaneous ceilometer–HBTM difference at night is 21%. Some significant instantaneous differences are examined in detail in section 4a.

Figure 9 shows the comparison of z_s^t and z^t for region 5. The correlation is best at night with $R = 0.36$, compared to $R = 0.19$ during the day. The rms cloud-top height difference during the day is 197 m, while at night it is 160 m. The poor comparisons of the instantaneous data are probably due to the use of a single lapse rate to compute z^t and to the use of the satellite-derived surface temperature to calibrate the lapse rate. The aircraft-measured, boundary-layer lapse rates varied from -5.5 to -9.8 K km^{-1}. Sometimes the surface air temperature differed from the sea surface temperature by as much as 2 K (Jensen 1990). Therefore, even if the lapse rate was always 7.1 K km^{-1}, there would be errors in the cloud-top height because the value of T_{sfc} was inappropriate to establish the vertical temperature profile.

Optical depth is proportional to LWP and, for the adiabatic approximation for shallow layers, LWP is proportional to the square of the layer thickness (e.g., Albrecht et al. 1990). Therefore, cloud thickness is correlated with $\tau^{1/2}$ in Fig. 10. The least-squares regression fit to the data shown in the figure is

$$\Delta z_s = -45.6 + 84.3\tau^{1/2}. \quad (1)$$

The correlation coefficient is 0.64. This fit produces no residual difference. The prediction of Δz using (1) yields an rms error of 61.6 m.

A comparison of $\log W_m$ with $\log\tau$ (Fig. 11) is less encouraging. For this fit, $R = 0.48$. The Stephens (1978) and Fairall et al. (1990) models are also plotted for comparison. The current fit yields

$$\log W = 0.601 + 1.11 \log\tau, \quad (2)$$

which is very close to the formula derived from the surface-based data (Fairall et al. 1990), as seen in Fig. 11. Nevertheless, these lines do not appear to fit the data very well. Since both W_m and τ depend on integrations of the cloud-droplet-size distribution, the droplet number density, and the cloud thickness, either quantity may be used as the independent variable. Therefore, a regression also was performed using $\log W_m$ as the independent variable. The geometric average slope and offset were computed using the results from both fits. Figure 12 shows the component and resultant regression lines. The geometric averaging yields

$$\log W = 0.109 + 1.60 \log\tau, \quad (3)$$

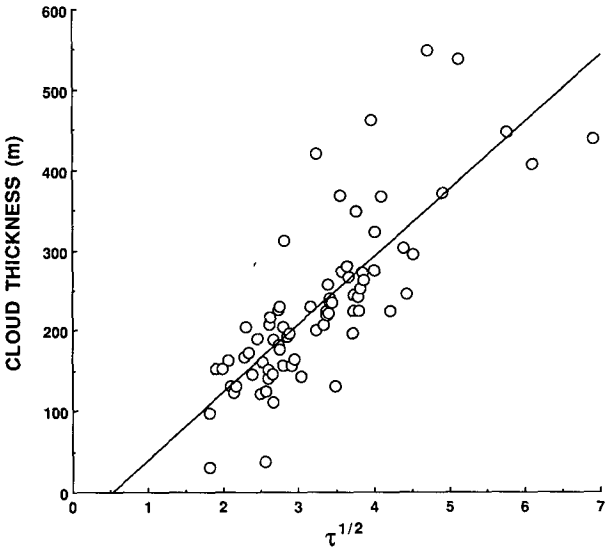

FIG. 10. Comparison of surface-derived cloud thickness and region 5, satellite-derived cloud optical depth, 1–19 July 1987.

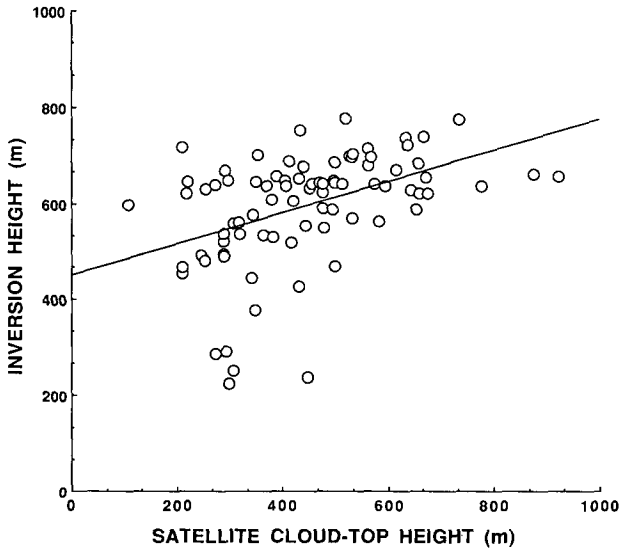

FIG. 9. Comparison of HBTM daytime, region 5, cloud-top heights and surface-observed inversion base heights, 1–19 July 1987.

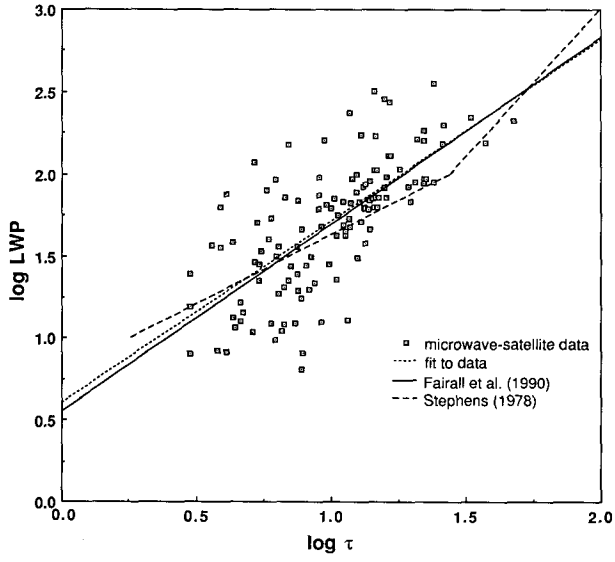

FIG. 11. Relationships of liquid water path to cloud optical depth. Data were taken over San Nicolas Island.

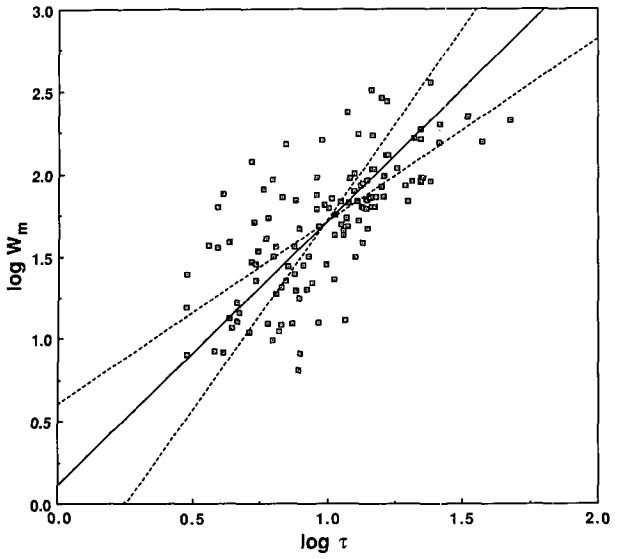

FIG. 12. Geometric mean, least-squares regression fit (solid line) to microwave LWP and GOES-derived cloud optical depth data (Fig. 11). Dashed lines denote the individual fits.

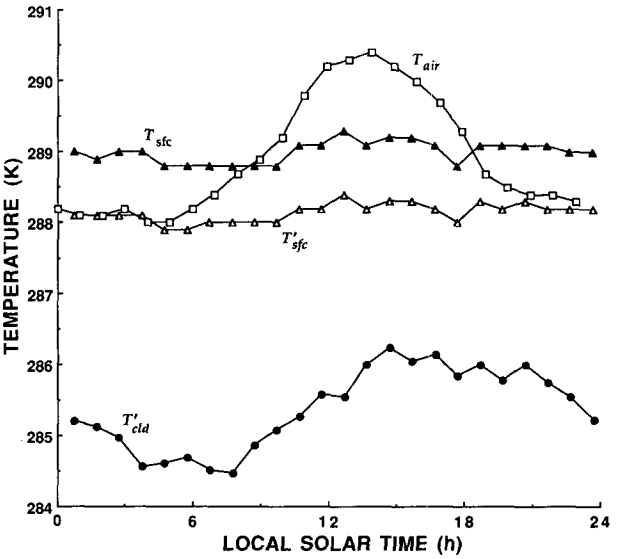

FIG. 13. Comparison of mean region 5 and site-observed air temperatures, 1–19 July 1987.

which appears to fit the data better than either component regression line.

Regression of W_m with W_r yields only $R = 0.61$ (Fairall et al. 1990). Spatial resolution differences are probably the largest source of error here because W_r is derived with a wide-field-of-view radiometer and W_m is computed from a beam measurement. The errors are expected to be worse for the correlation of the instantaneous regional satellite data with the time-averaged point measurement. Another source of error may be the use of plane-parallel radiative transfer results to interpret the satellite-observed bidirectional reflectances. There is considerable uncertainty in the instantaneous anisotropy of the cloud-reflected radiation field because of optical depth and cloud-geometry variations. Time and space averaging of satellite measurements is generally assumed to diminish optical depth errors caused by the anisotropy uncertainties.

c. *IFO hourly averages*

Comparison of instantaneous data taken at dissimilar resolutions is unsatisfactory for estimating the relative differences. Further time averaging of the data should provide for a better assessment of the differences between the satellite and surface observations. A comparison of the mean diurnal variations in temperatures at SNI and for region 5 are plotted in Fig. 13. The surface air temperatures T_{air} taken at the surface site are adapted from Blaskovic et al. (1990). Corrections of T'_{sfc} for water vapor attenuation of the IR radiance are approximately 1 K. The diurnal variation in the resulting surface skin temperature is ~0.5 K, compared to a 2.5 K range in the mean air temperature. Mean values of T_{air} and T_{sfc} are almost identical. The variation in the mean corrected cloud-top temperature is nearly 2 K, with a maximum value at 1500 LST and a minimum just after sunrise.

Figure 14 shows the hourly mean cloud amounts during the IFO from both the island and the region 5 satellite data. Only data having values from all three cloud analyses are included in this figure. Before sunrise, the HBTM cloud amount generally falls around

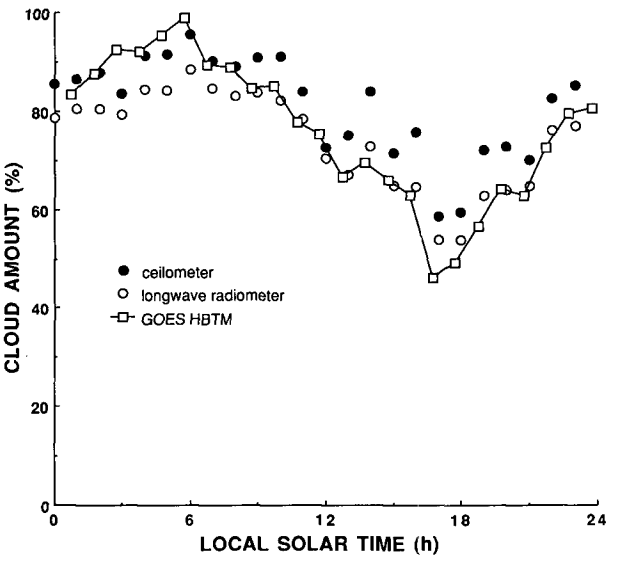

FIG. 14. Comparison of mean hourly, GOES-derived cloud amounts for region 5 and mean hourly, surface-based cloud amounts derived from measurements taken from San Nicolas Island, 30 June–19 July 1987.

the ceilometer values. The region 5 data correspond most closely to C_r during the day, tending to be slightly lower, on average. In almost all cases, $C < C_c$ during the day. The average and rms values of the hourly means for $C - C_c$ are -5% and 8%, respectively. For the radiometer cloud amounts, the mean and rms differences are 2% and 6%. These smaller differences may be the result of the greater spatial coverage of the radiometer and the effect of the surface site. For instance, the radiometer is influenced by the clouds or open skies over the water surrounding the surface site on the northwestern point of SNI, whereas the ceilometer detects cloudiness only directly overhead. Cloudiness tends to be less over the water northwest of SNI than over water to the southeast. For example, the average cloud amounts shown in Fig. 15 for regions 1, 5, and 9 along the mean wind vector indicate that cloudiness over the water northwest of SNI breaks up rapidly and more completely than it does just southeast of the island. It also takes longer for the clouds to redevelop during the night. The cloud cover over region 9 corresponds much more closely to C_c (difference of -3%) than it does to C_r (difference of 5%). The cloudiness over the surface site may be more typical of region 9 (southeast of the island) or it may be locally influenced. Potential local influences are discussed in the next section. If the radiometer data are used as a reference, it may be concluded that the HBTM cloud amounts are accurate to within $\pm 5\%$ on an hourly mean basis.

Figure 16 compares the hourly mean cloud heights derived from the satellite and the surface. The diurnal range in z_s^t is 225 m, with a maximum at local noon and a minimum at 1700 LST. The maximum in z^t occurs around 0800 LST, with a broad minimum between 1400 and 2200 LST. The range in z^t is 210 m. If the nonblackness of the clouds is taken into account with the cloud emissivity correction, the diurnal range in z^t reduces to 200 m. The emissivity corrections are significant only during the afternoon. Unfortunately, the emissivity correction is limited to the daytime, precluding its general application. Even without the correction for ϵ, the satellite provides a relatively accurate depiction of the diurnal variation of cloud-top height despite the poor instantaneous correlations found earlier. On average, z^t is 53 ± 77 m lower than z_s^t.

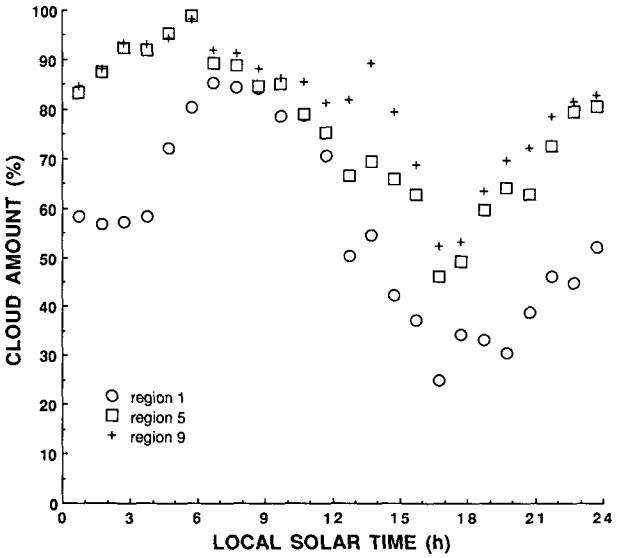

FIG. 15. Comparison of regional (see Fig. 1) mean hourly cloud amounts derived from GOES data using the HBTM, 30 June–19 July 1987.

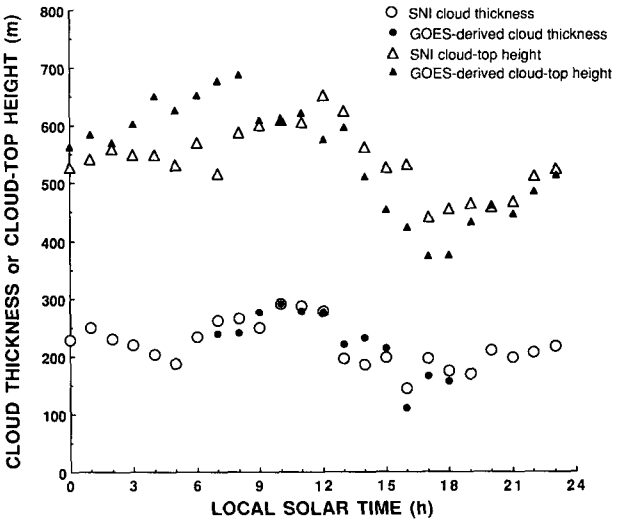

FIG. 16. Comparison of mean hourly cloud-top height and cloud thickness data taken on 1–19 July 1987. Surface and GOES data taken over San Nicolas Island and region 5, respectively. SNI cloud-top height is assumed to be the measured inversion base height.

Mean hourly cloud thickness derived with (1) is also compared with SNI cloud depth in Fig. 16. Both the satellite and surface observations yield maximum thickness of ~290 m around 0945 LST. There is a surface-observed minimum of ~150 m during the late afternoon. The mean and rms differences between Δz and Δz_s are 3 and 23 m, respectively. Again, the satellite retrieval requires visible data to infer cloud thickness, so application of this method is limited to daytime data.

Mean cloud optical depth is shown in Fig. 17. The GOES data produce a peak in τ of 15.6 at 0945 LST, corresponding to the maximum thickness (Fig. 16). The steady decrease in τ during the afternoon is similar to that seen for the entire grid, except that the optical depth in this figure begins to rise again before sunset. The data presented here are only for those times when both satellite and matching surface data were available. This matching process results in irregular sampling. Figure 17 also compares the mean liquid water path derived from the microwave and solar radiometers and from (3) using the satellite data. The weak correlation found with the instantaneous data shows up here with differences in the times and magnitudes of the daytime

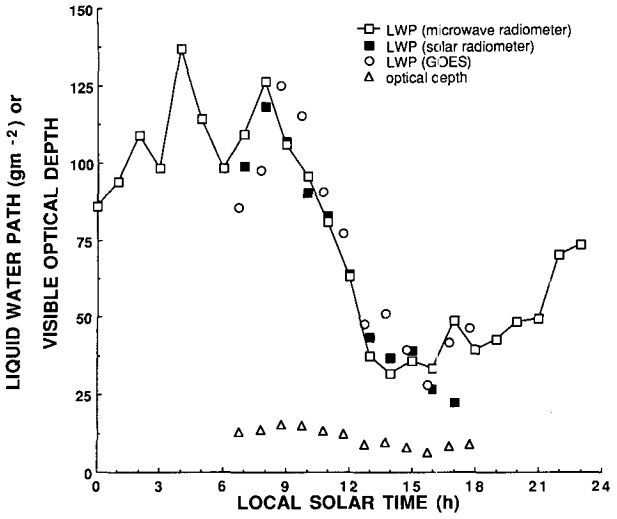

FIG. 17. Mean hourly cloud liquid water path and optical depths, 1–19 July 1987. Surface and GOES data taken over San Nicolas Island and region 5, respectively.

peaks in W derived from the satellite and the surface observations. Overall, the average hourly mean and rms differences between W and W_m are 2.7 and 16 g m^{-2}, respectively. The maximum in W_m occurs about 1 h before the peak value of W. The latter corresponds to the optical depth maximum. The phase shift in these maxima may be due to the model used to interpret the radiances or to microphysical differences between the cloud and the model cloud. The close correspondence of τ with Δz, however, is consistent with a maximum in integrated liquid water path at 1000 LST. The microphysical aspects of the apparent differences in the diurnal variations of liquid water path are discussed in section 4c.

4. Discussion

a. Cloud amounts

One of the goals of this study is to estimate the uncertainties in the various satellite-derived cloud properties, but a straightforward assessment is not possible because of differences in scale between the island and satellite-based instrumentation. There were significant instantaneous discrepancies and some mean hourly biases, however, that should be explored further to determine if the primary source of the differences is the algorithm or the scale dissimilarities.

The underlying assumption in this comparison is that the mean cloudiness over the surface site is the same as that found over region 5. It is implicit that the averages will be the same because the clouds pass at random over a given position within the box containing the island. At a given instant, there will be differences between the region 5 cloud fraction and the island cloud fraction because of random variations in the cloud field. Given the mean wind speed of ~5.5 m s^{-1} (Blaskovic et al. 1990), the clouds passing over the island traverse a distance roughly equal to one-half of a 0.33° grid box during an hour. Since 2 h are required for a cloud field observed over SNI to traverse the box, one measure of the random variations of cloudiness over the island relative to the box is the hour-to-hour difference in the ceilometer cloud fractions. The rms hour-to-hour difference in the ceilometer cloud amounts is 18%. This difference is nearly the same as the rms difference of 17% between the satellite and ceilometer cloudiness. Thus, the random, instantaneous differences between C and C_c can be attributed to large-scale effects.

Considering the 334 instances when both the ceilometer and the HBTM recorded a cloud amount and the hour-to-hour differences in C_c, the standard error in the mean region 5 cloudiness based on C_c is ±1%. Since the mean difference between C and C_c is 5%, either C is biased or the surface-site cloudiness is not representative of the region 5 cloud amount. To examine this latter possibility, the satellite imagery was examined in detail using video loops provided by D. P. Wylie of the University of Wisconsin–Madison (personal communication, 1988) and still photographs of 1-km images. The video loops were used to obtain a general overview of the variations in the clouds around the island. Subjective analyses of the video imagery revealed that during the days when the cloud cover dissipated, it typically dispersed around, but not over, the island first and rebuilt over the island more quickly than over the surrounding water. Clearing of various degrees occurred around the island but not over its northwestern tip during 2, 7, 10, and 11 July. During 5 days of the period, a clearing or thinning appeared in the shape of the letter V, with its apex over the island

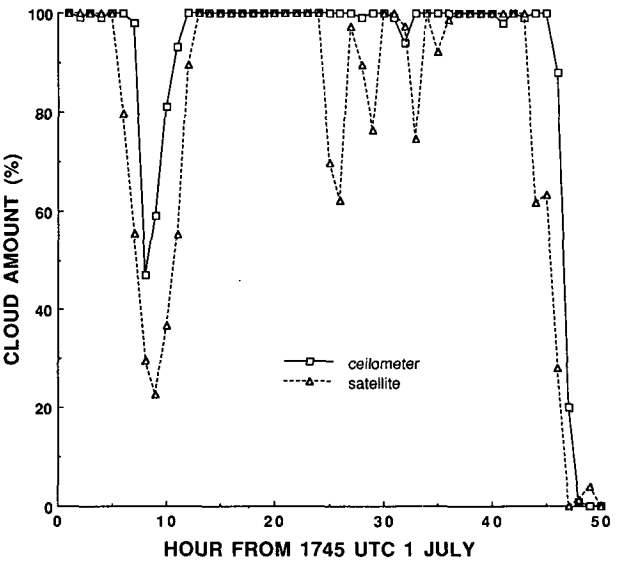

FIG. 18. Hourly cloud amounts over SNI and region 5, 1–3 July 1987.

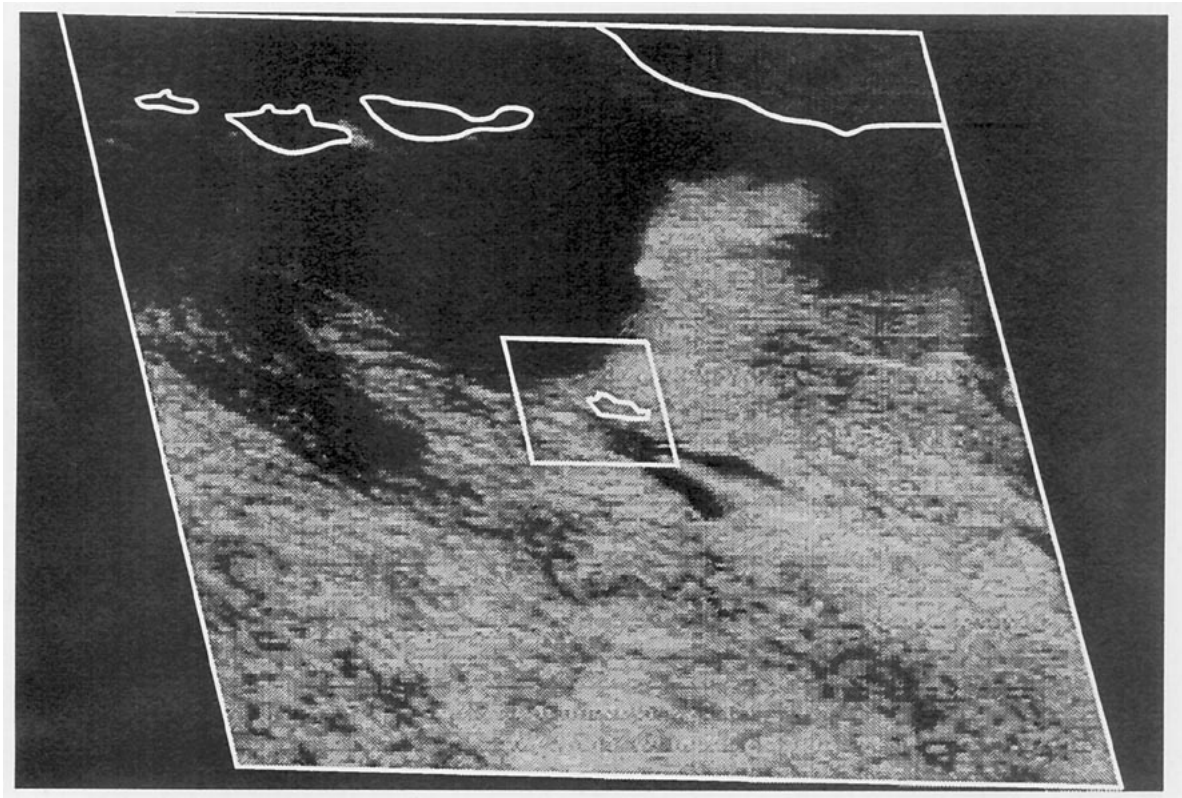

FIG. 19. Visible, 1-km GOES image showing region 5 and a map of SNI, 0045 UTC 2 July 1987.

and with the clearing southeastward from the island. These V patterns broke down into extensive clearings during 1 and 3 July. They also occurred during 13 and 14 July but resulted in no appreciable clearing.

Figure 18 shows a time series of C and C_c for the first 3 days of the comparison period. During the afternoon of 1 July, the clouds start breaking up around the island 1 h earlier than over the ceilometer site. A cloud-free area north of the island contributed to some of the satellite-observed clearing, as seen in Fig. 19 taken at 0045 UTC 2 July. The V pattern is very evident this day. The poor navigation of the satellite data is also apparent in this image, where the map overlay is based on the actual navigation calculations. Here, SNI is located under the clouds west-southwest of the map island. For this case, C is 80%, compared to 100% for C_c. Redevelopment of the cloud field over the whole region is slower than over the island. The clouds lingered around the northern half of the island throughout the afternoon of 2 July, while holes in the regional cloud field came and went. On the following day, the northern clear area and the V pattern reappeared and gradually merged, resulting in total clearing of the region, consistent with the results in Fig. 18.

Another time series taken between 5 and 7 July is plotted in Fig. 20. The relative dissipation and growth of the cloud field during 5 July is consistent with the video loops, which show that the cloud deck disappears entirely by 2345 UTC. During 6 July, the regional and ceilometer cloud amounts are more consistent, with less tendency for an "island effect." Figure 21a shows the image for 1945 UTC 6 July when C is 44% and C_c is 11%. The navigation is slightly worse than that in Fig. 19, although the island is still in the box. In this case, the clouds east of SNI were not detected by the

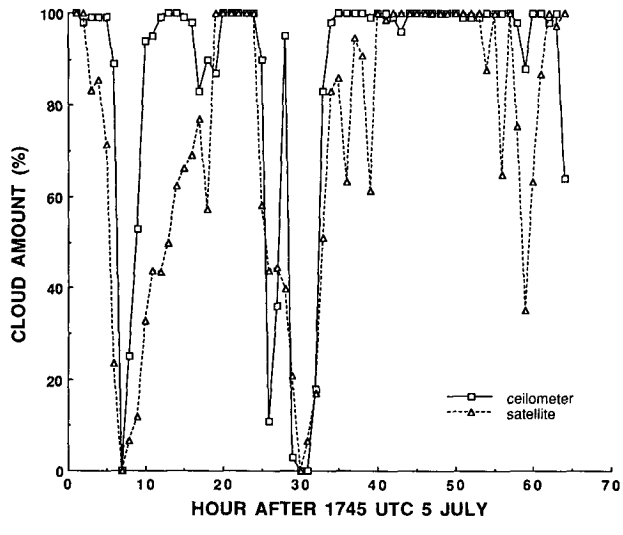

FIG. 20. Same as Fig. 18, but for 5–8 July 1987.

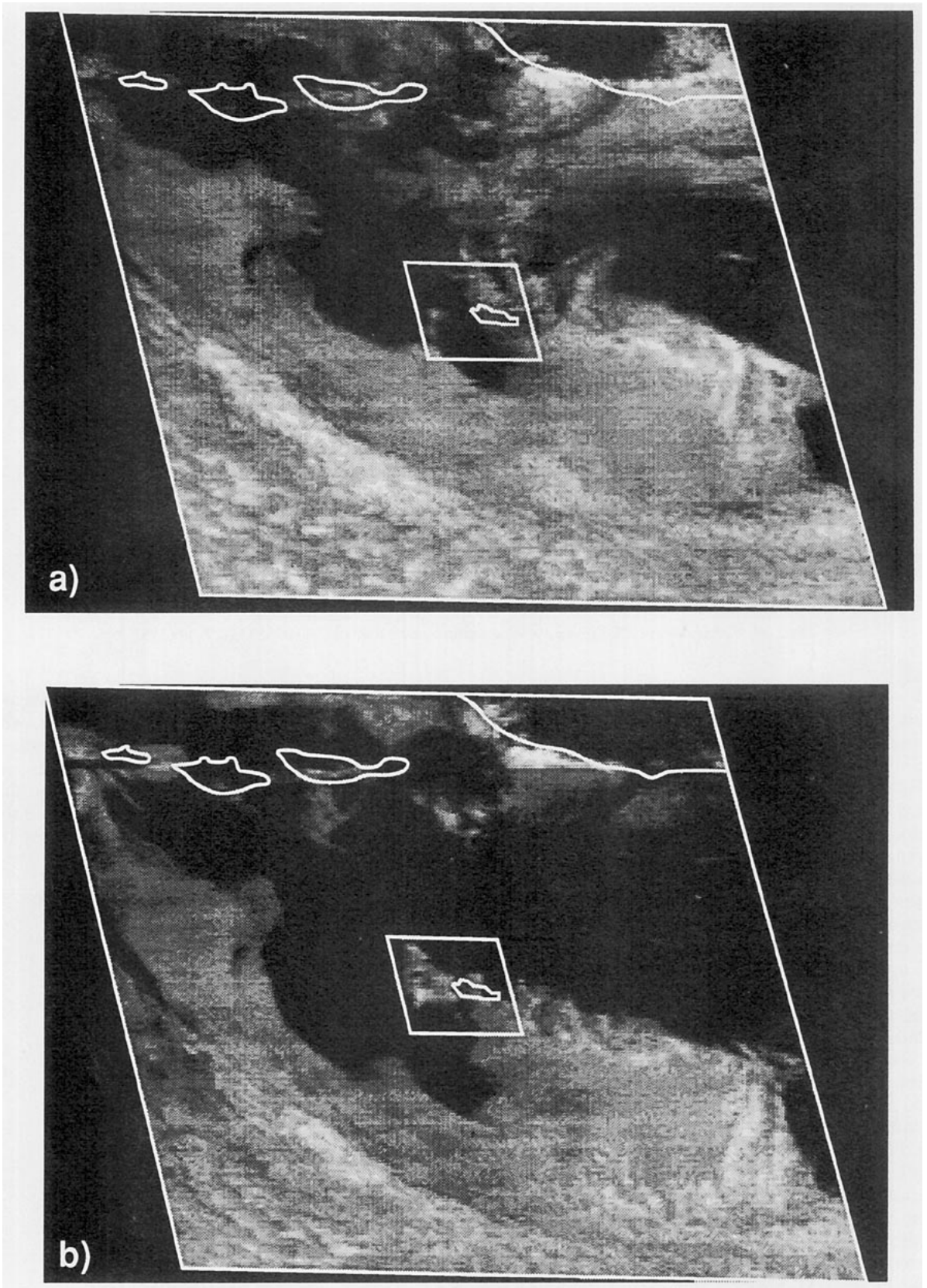

FIG. 21. Same as Fig. 19, but for 6 July 1987; (a) 1945 UTC, (b) 2045 UTC, (c) 2145 UTC, (d) 2245 UTC.

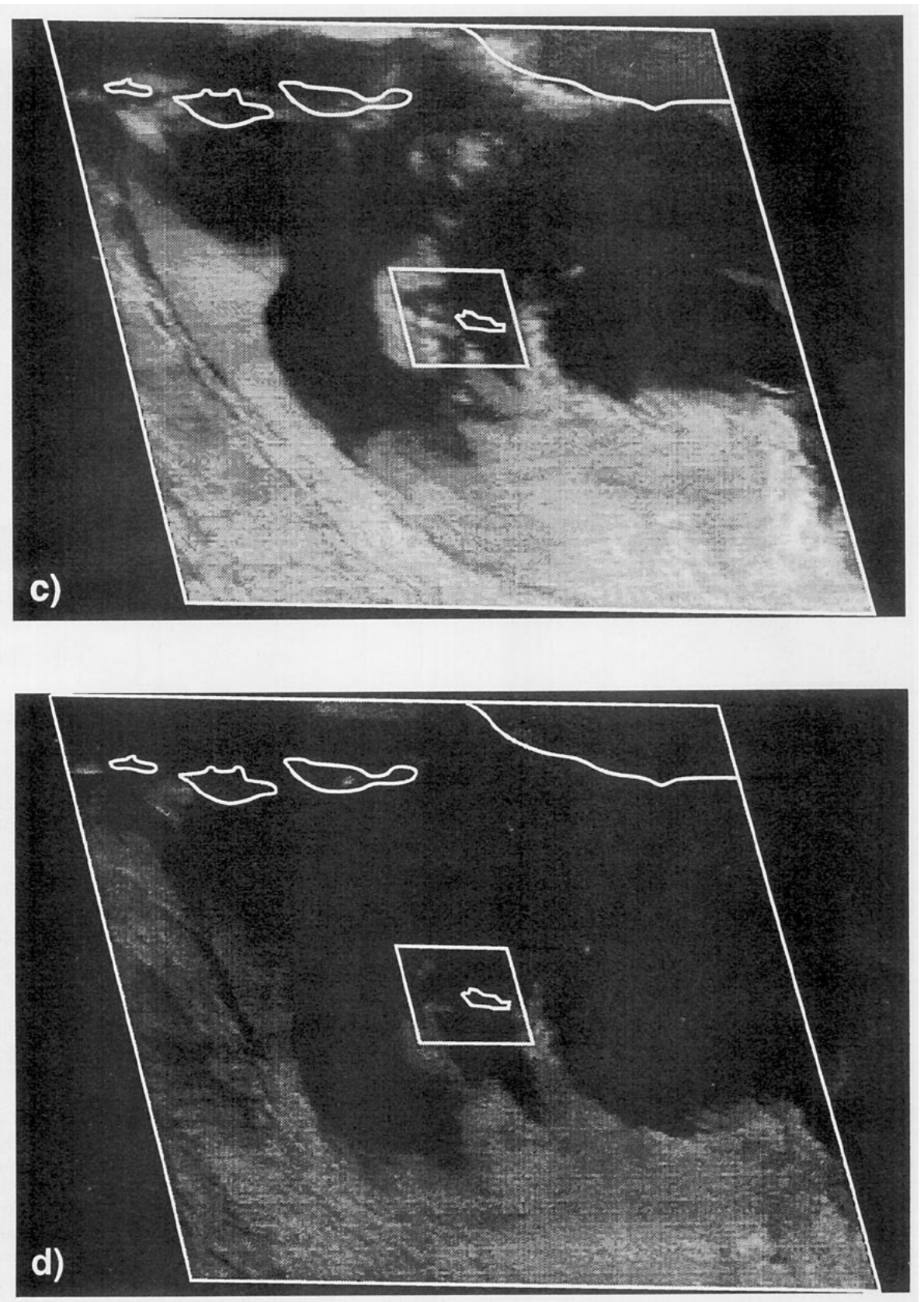

FIG. 21. (*Continued*)

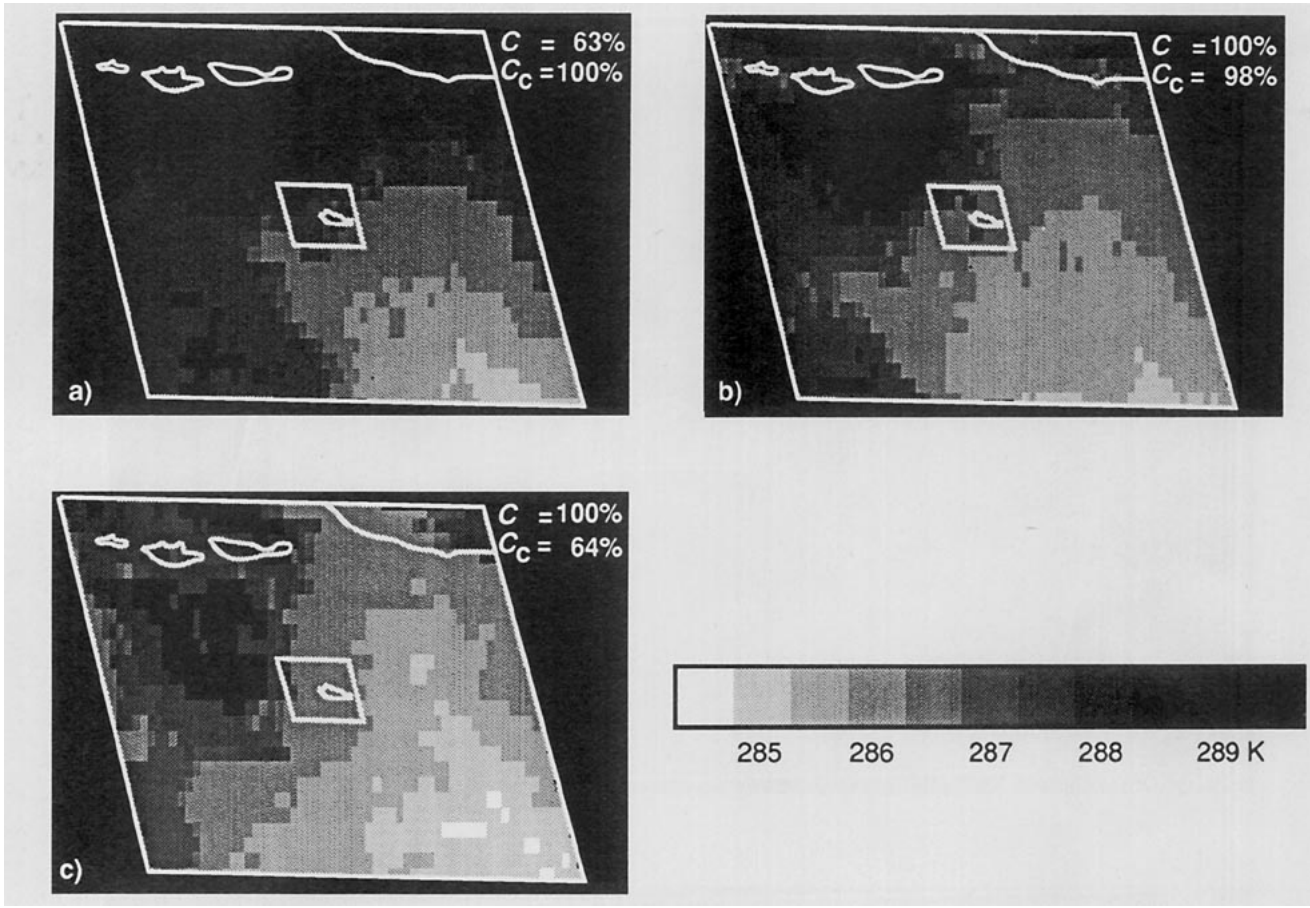

FIG. 22. Infrared, 4-km image showing region 5 and a map of SNI, 8 July 1987; (a) 0545 UTC, (b) 0745 UTC, (c) 0945 UTC, (d) 1045 UTC, (e) 1145 UTC.

ceilometer, which observed the small cloud deck seen just off the northwestern tip of the actual island. From the video loop, the cloud-level winds appeared to be east-northeasterly, so that the cloud mass in the eastern part of box reached the island the following hour (Fig. 21b) when the surface and satellite cloud amounts were much closer. The next hour, as the same cloud mass continued westward out of the box (Fig. 21c), C_c is 91% compared to 40% over region 5 (Fig. 20). The clouds continued to dissipate and move out of the box (Fig. 21d), resulting in C_c of 3% and C of 21% at 2245 UTC. During the following day, the V returned for a few hours, with no apparent clearing over the island. Cloud-free areas north and east of the island entered part of region 5 late in the afternoon, causing some decreases in C.

Some clearing apparently occurred between 0245 and 0745 UTC 8 July, which was generally unobserved by the ceilometer. The ceilometer, however, detected cloud-free skies for part of the time between 0945 and 1045 UTC when region 5 was determined to be overcast by the HBTM. Figure 22 shows the IR imagery used by the HBTM at several of the times when discrepant cloud amounts were found. Satellite and ceilometer cloud fractions are also given. The sequence of pictures shows an apparent buildup of clouds from the east, which gradually reduces the dark clear area. In region 5, the temperature ranges from 286 K in the southeastern corner to 288.5 K in the northwest at 0545 UTC. By 0745 UTC, the maximum temperature is 287.5 K, and it remains at that value through 0945 UTC. The maximum temperature then drops for the next 2 h to 287 K at 1045 UTC and 286.5 K at 1145 UTC. The minimum temperature remains steady at 286 K throughout the night. Cloud amounts computed from the satellite data are consistent with this series of images. The clear area in the northwestern part of the region at 0545 UTC is gone by 0745 UTC and does not reappear. The surface cloudiness variations are difficult to explain with this set of imagery. Either the clouds are forming preferentially around the island at one time and clearing preferentially at others or there are problems with the navigation. The first option is not inconceivable given the analysis of the video loops. The apparent size of the cloud holes detected by the ceilometer should be sufficient to produce a tempera-

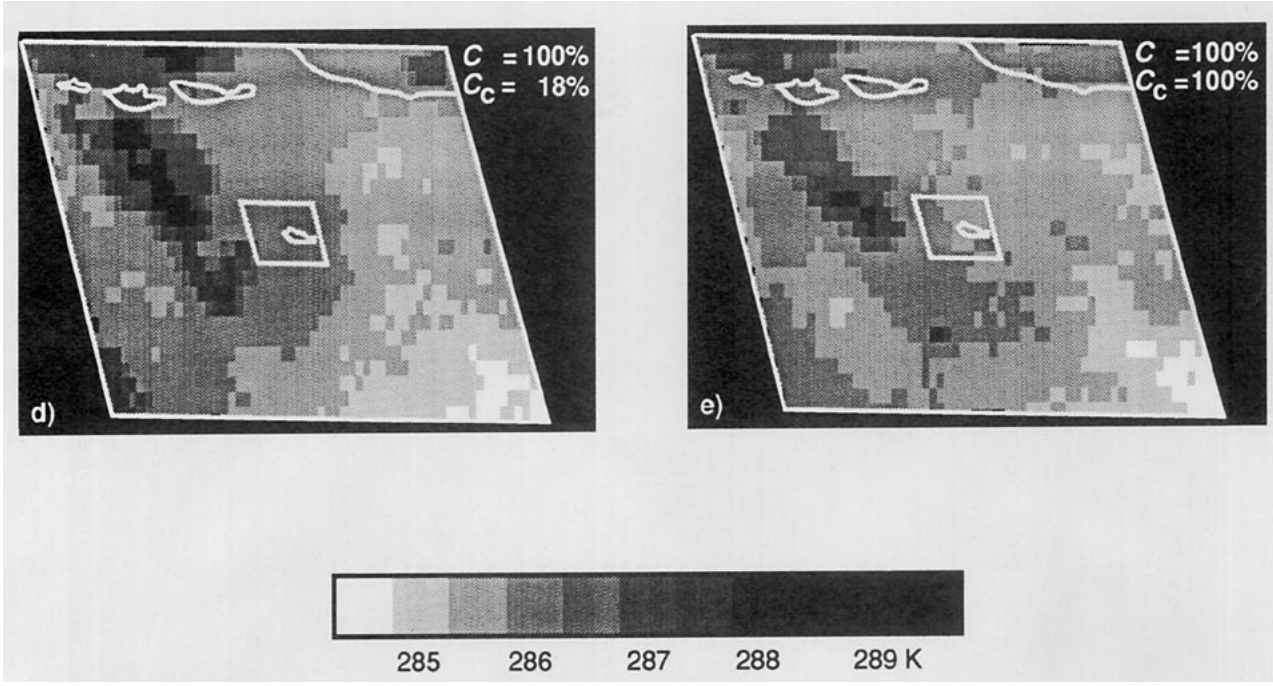

FIG. 22. (*Continued*)

ture increase if the clouds and clear areas differ in temperature by more than 1.5 K, as seen at 0545 UTC. No holes are evident over region 5 in Figs. 22d,e. The navigation error is more likely to be the source of the discrepancies. From VIS imagery taken earlier in the day, the offset in the islands would place the tip of SNI at the left edge of the box below the center line. At that location in the images, the surface site would be in the tip of a small cloud mass at 0545 and 0745 UTC, at the edge of the clear area at 0945 and 1045 UTC, and completely within the larger cloud field at 1145 UTC. Cloud amounts in the adjacent grid box, region 4, were 49%, 32%, 0%, 64%, and 54%, corresponding to Figs. 22a–e, respectively. Thus, these particular differences in the cloud fractions are probably due to poor navigation of the satellite data.

The case of clouds dissipating around the island but not over it is typified in Fig. 23, which compares the surface and ceilometer cloud amounts for 10–12 July. Very little clearing is evident in the ceilometer results, whereas the region 5 cloudiness breaks up during both afternoons. Visible images for 2345 UTC 10 July and 2345 UTC 11 July are shown in Figs. 24a and 24b, respectively. In the former case, SNI is overcast with large clear areas around it (note the navigation offset). The following day, a clearing zone moves toward SNI from the east, with some openings forming on the southwest side of the island. Apparently, the large clearing reached SNI around 0345 UTC 12 July before the cloud deck formed again (Fig. 23).

The relative underestimates of cloud fraction by the HBTM in Fig. 25 during the early morning of 17 July appear to be due to the algorithm rather than navigation or scale differences. In all cases during the period 0145–1345 UTC 17 July, the maximum temperature does not exceed 283 K, whereas the clear-sky temperature is ~286 K. Because of the small contrast between the surface and the clouds in this case, an alternative HBTM method (Minnis et al. 1987) was used, which caused the underestimate. During the remainder of 17 and 18 July, the two cloud amounts compare favorably,

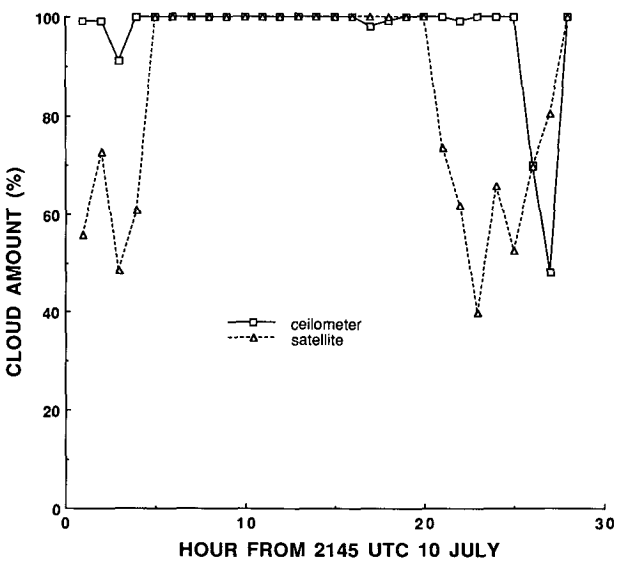

FIG. 23. Same as Fig. 18, but for 10–12 July 1987.

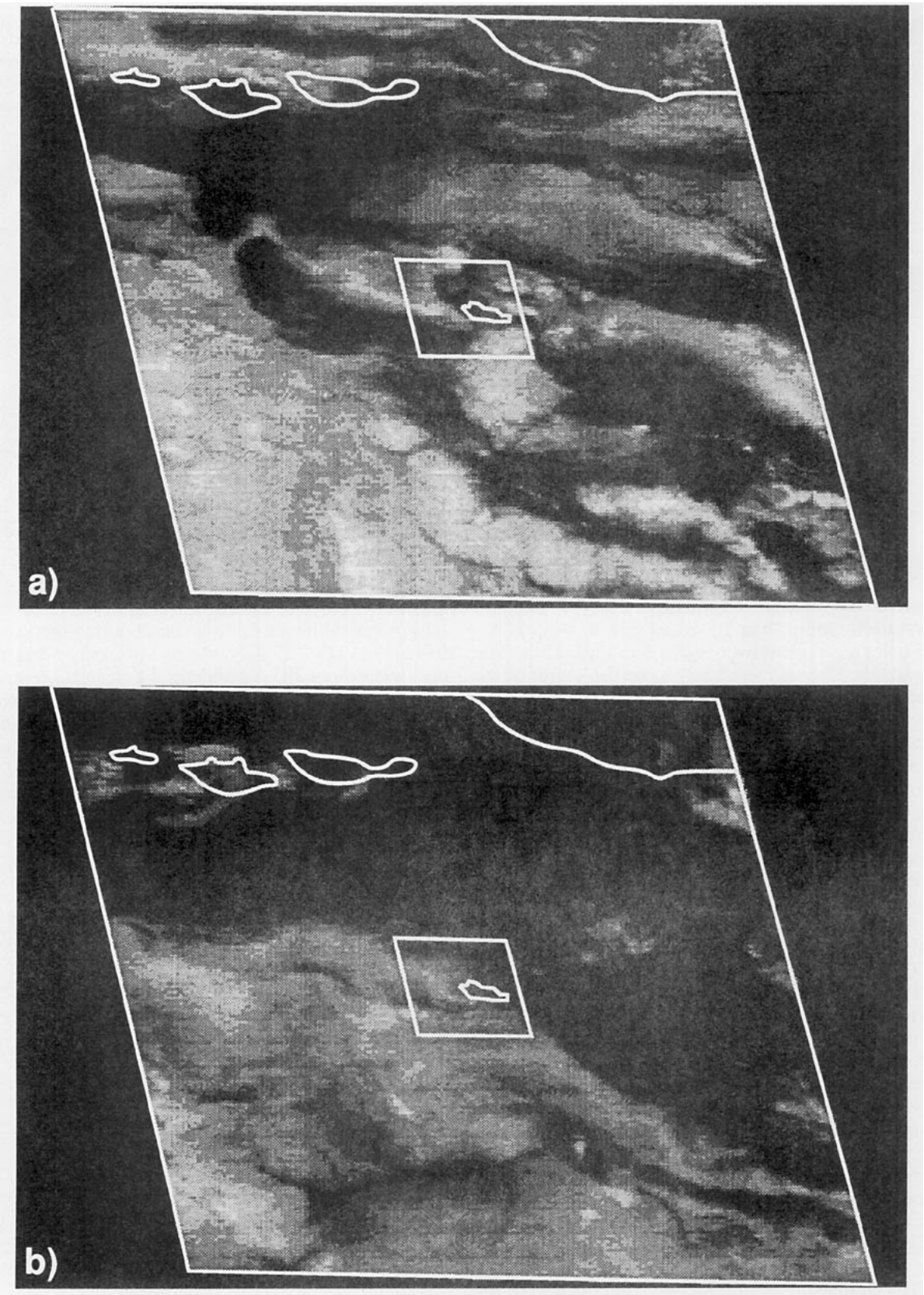

FIG. 24. Same as Fig. 19, but for (a) 2345 UTC 10 July 1987 and (b) 2345 UTC 11 July 1987.

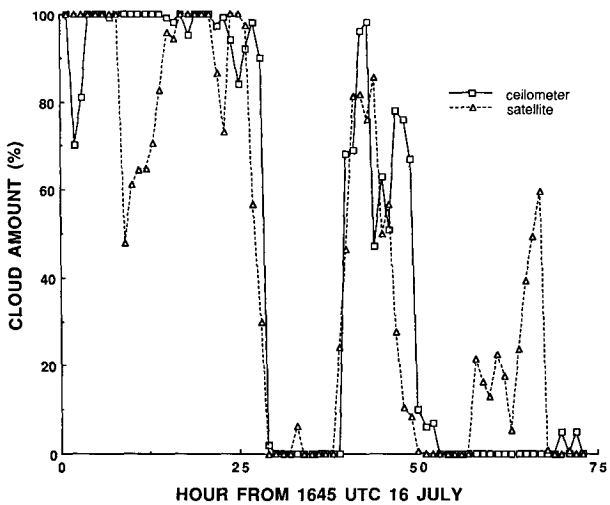

FIG. 25. Same as Fig. 18, but for 16–19 July 1987.

except for the usual island effect during the afternoons. The HBTM detected cloudiness between 0345 and 1245 UTC 19 July, which was not evident in the ceilometer readings. This apparent cloudiness is seen in Fig. 26, which shows the IR imagery for 1245 and 1445 UTC. Figure 27 shows the VIS imagery for 1445 UTC, when the satellite-detected cloud fraction was only 1%. The island is in the box but southwest of the map island. Very few clouds are evident in the box in Fig. 27, although a rather extensive, thin deck is west and southeast of the region. The edge of this deck is associated with $T = 286$ K, indicating that pixels having this value are probably partly cloudy. The actual distinction between clear and cloudy areas, however, is ambiguous. According to the values of VIS reflectance at 1445 UTC, there are clear pixels in region 5 that have $T = 286$ K and some cloud-contaminated pixels that have $T = 286.5$ K. The maximum value of T is 287.5 K throughout the night and early morning. At 1245 UTC, the minimum temperature is 285.5 K, compared to 286 K 2 h later. Because of the relative temperatures and their ranges at these 2 h and earlier times from 0345 UTC, it is concluded that a significant amount of cloudiness passed through the grid box during the night. The exact amount is unknown, but it probably did not reach as high as the 60% recorded at 1245 UTC. No cloudiness was detected at the island because the clouds appeared to be located south and east of the true island location. This case represents an extreme test for any IR threshold algorithm because there is so little contrast between the clear and cloudy scenes. In these situations, the HBTM can either under- or overestimate the cloud fraction. During the morning of 19 July, the algorithm probably overestimated the cloudiness, whereas it underestimated the cloudiness during the morning of 17 July (Fig. 24). Such compensating effects result in good agreement between the mean satellite and ceilometer cloudiness at night (Fig. 14).

From this discussion and the supporting imagery, it was found that much of the random difference between the satellite and ceilometer cloudiness is due to the scale effects and navigation error. The latter does not contribute significantly to any of the mean difference because the satellite navigation error appears to be primarily in the longitudinal direction. In this direction, the satellite-derived mean cloud cover ranges from only

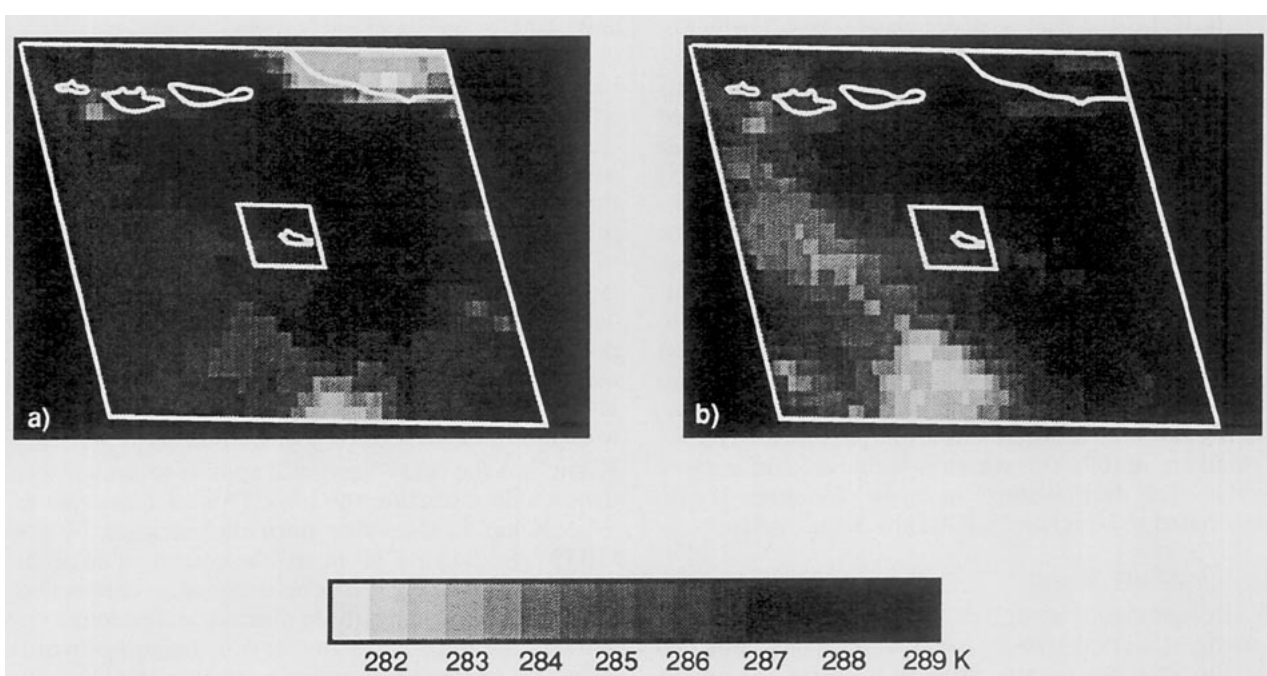

FIG. 26. Same as Fig. 22, but for 19 July 1987; (a) 1245 UTC, (b) 1445 UTC.

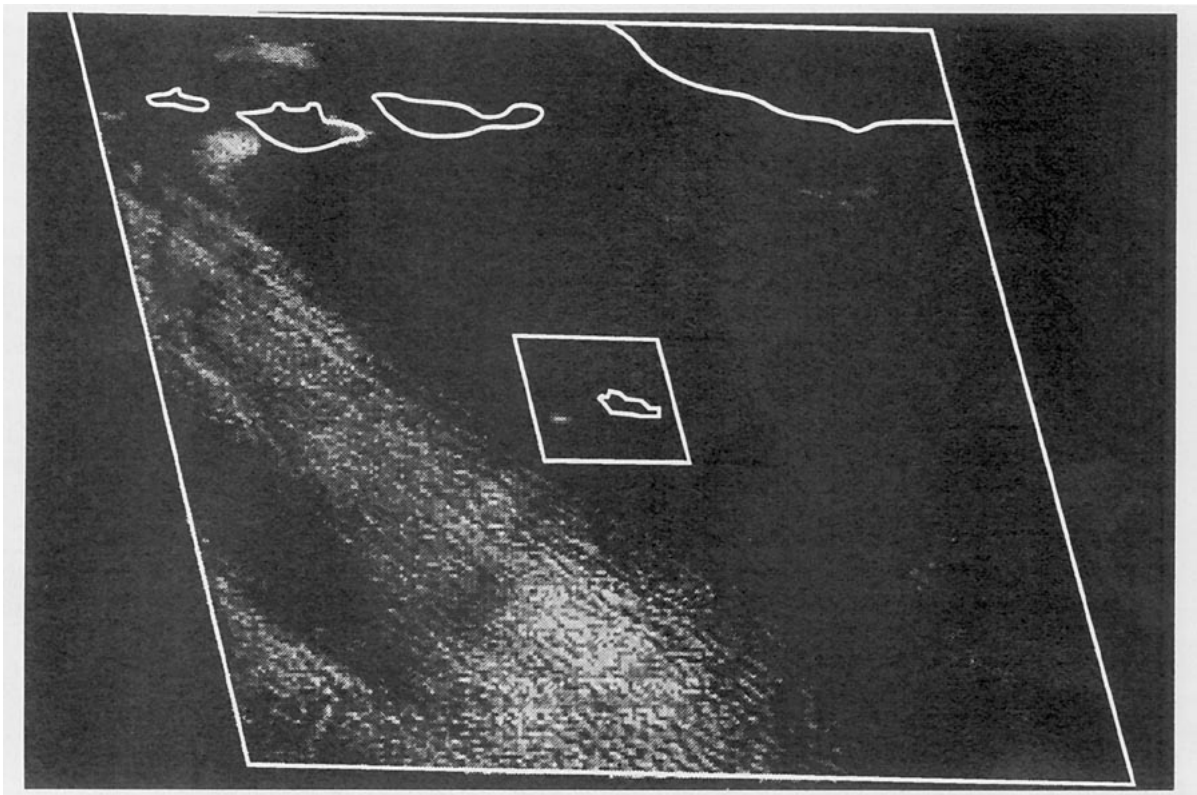

FIG. 27. Same as Fig. 18, but for 1445 UTC 19 July 1987.

72% to 73% for regions 4–6. It is concluded that the bias between the average cloud amounts is primarily the result of an island effect, which is characterized by persistence of cloud cover over SNI during several periods of clearing over adjacent water areas. The major clearings occurred during the day, when most of the bias is observed. At night, the mean cloud amounts are nearly equal. The assumption that the surface-based cloud amounts are representative of the region is, therefore, only partially true. Qualitatively, the HBTM results provide a very reasonable representation of the cloud-cover variations within the environs of SNI. The HBTM cloud amounts are as accurate as can be determined from the ceilometer data and satellite imagery. The island effect is probably large enough to account for all the 5% difference between the HBTM and ceilometer cloud amounts, but its magnitude cannot be determined exactly. Given these comparisons, it is conservatively estimated that the mean HBTM cloud amount for this region is within ±3% of the true value. The diurnal range in mean cloudiness is also estimated to be within ±3% of the actual value.

b. Cloud-top heights

Instantaneous errors in cloud-top height are primarily attributable to the use of a single lapse rate tied to the sea surface temperature in the satellite analysis. Hourly rms differences in the inversion height are only 50 m, compared to an rms difference of 212 m between z' and the inversion height. The 53-m mean difference can arise from several sources, such as the location of the actual radiating center of the cloud, the assumed lapse rate, or an island effect.

As explained by Cox and Griffith (1979), the nebulosity of the cloud causes the observed radiometric temperature to correspond to some finite depth in the cloud, which depends on the density of the cloud particles. For instance, Cox and Griffith (1979) estimated that the radiometric temperature of a cloud at 950 mb in the tropics would correspond to the temperature ~20 m below the physical top of the cloud. The relationship in Fig. 10 and its use in (1) suggest that the depth required to attain blackness is probably greater than 20 m. Another consideration is the effect of the assumed lapse rate. For example, a change of only 0.6 K in the mean lapse rate applied to the satellite data would eliminate the bias. Thus, a lapse rate of −6.5 K km^{-1} in the mean lapse rate applied to the satellite data would eliminate the bias. Thus, a lapse rate of −6.5 K km^{-1}, the value normally assumed by the HBTM, would have produced the correct value of the mean cloud-top height. The existence of an island effect on cloud-top height is more difficult to determine because of the uncertainty involved in assigning an altitude to a temperature in low-contrast conditions exemplified by Fig. 26. During a few days, there appeared

to be a thickening (brightening) of the clouds over the island in the VIS video loops, but attempts to relate this to temperature decreases were unsuccessful. From the available information, it is concluded that the mean difference between the surface and satellite cloud-top heights is probably due to the algorithm.

The relationship for cloud thickness derived here may be applicable only to the clouds in the SNI area if they are not representative of a typical stratocumulus cloud. Further comparisons with FIRE aircraft results and other surface observations would be needed to determine the general applicability of this formula. Other types of clouds at higher altitudes and having other droplet-size distributions may have a different relationship between thickness and optical depth. The present results are very encouraging, however, for estimating cloud thickness. Knowledge of the thickness and the cloud-top height would allow a better estimate of cloud base than is currently available from satellites.

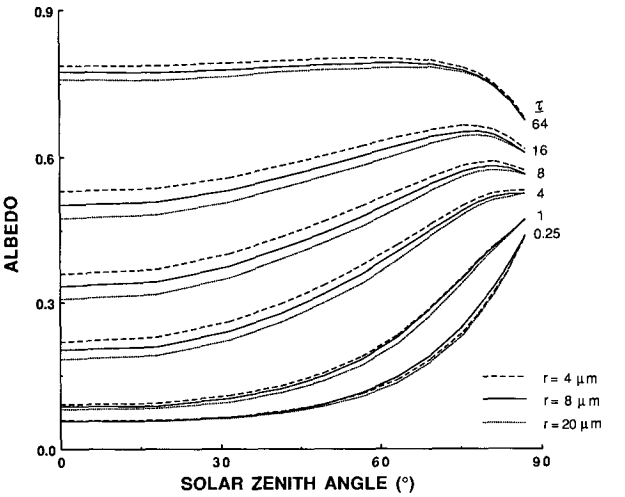

FIG. 28. Variation of theoretical, top-of-the-atmosphere albedos over ocean for clouds having various effective droplet radii.

c. Liquid water path and optical depth

The estimations of liquid water path and cloud thickness from the cloud optical depth are based on the assumptions that the clouds are plane-parallel sheets and have a fixed droplet-size distribution that corresponds to an effective radius of $r = 8$ μm. Fully overcast stratus clouds may fit the plane-parallel assumption more than most other types, but they still may have some cellularity, in addition to other horizontal and vertical inhomogeneities. Stratocumulus clouds, by definition, are cellular. Thus, cases with $C < 100\%$, probably stratocumulus, are less likely to fit the plane-parallel model than are the overcast cases. In either case, there will be some uncertainty in the satellite-retrieved optical depth because of violations of the plane-parallel assumption. Such uncertainties should be minimized for large cloud amounts.

The value of derived optical depth is also influenced by the effective droplet radius. To evaluate this effect, the adding–doubling calculations were performed for droplets having effective radii of 4, 12, 16, and 20 μm. The results from the radiative transfer calculations were used to construct lookup tables of reflectance versus optical depth for those effective radii, in addition to that already established for $r = 8$ μm. Figure 28 shows the sensitivity of the 0.65-μm albedo to droplet size and optical depth. The albedos for $\tau = 0.25$ are close to those for clear-sky conditions. There is little change in α with θ_0 for $\tau = 64$. Decreases in α for larger values of τ and θ_0 arise from enhanced ozone pathlengths and multiple scattering in the cloud. Convergence of the albedo values for $\theta_0 > 80°$ greatly increases the uncertainty of the retrieved optical depth at high solar zenith angles. For clouds of intermediate depth, the uncertainty in albedo due only to variations in r for a given optical depth ranges from almost 0.07 at overhead sun to 0.04 at $\theta_0 = 70°$. Converting those uncertainties in albedo to optical depth indicates that the optical depth derived using $r = 8$ μm may be in error, on average, by as much as 15% for a cloud having $r = 4$ μm. Since reflectance, not albedo, is used to infer optical depth, much greater errors may be realized at some angles (e.g., Nakajima and King 1990).

To better understand the combined optical depth–liquid water path dataset, the approximation

$$r \approx \frac{3}{2}\frac{\tau}{\mathrm{LWP}'} \tag{4}$$

(e.g., Slingo 1989) was used to infer the effective radius from the combined W_m and satellite-reflectance data. The mean effective cloud-droplet radius was determined for a given scene by iterating (4) using interpolations from the r-dependent lookup tables to estimate optical depth from the region 5 satellite reflectance and the corresponding microwave radiometer liquid water path measurement.

The results of the iterative calculations are shown in Fig. 29. This figure also includes in situ microphysical measurements taken during the IFO from a tethered balloon over SNI (Duda et al. 1989), from an aircraft flight directly upwind of SNI (Jensen 1990), and from a C-130 aircraft sampling stratocumulus clouds 60–120 km west and southwest of SNI (Rawlins and Foot 1990). Two groups of data are given for each balloon flight. The higher values correspond to estimates of the mean volume-effective radius of the droplets for the flight. The lower symbols correspond to the mean radius. Both values are given to bracket the satellite-surface results. Jensen (1990) reported only mean radius. Rawlins and Foot (1990) reported effective radius measured at various vertical locations in the clouds; the values were used to estimate the mean effective radius for the entire cloud. All of the plotted in situ values are averages for the entire flight. For example, the tethered-balloon data for 8 July represent

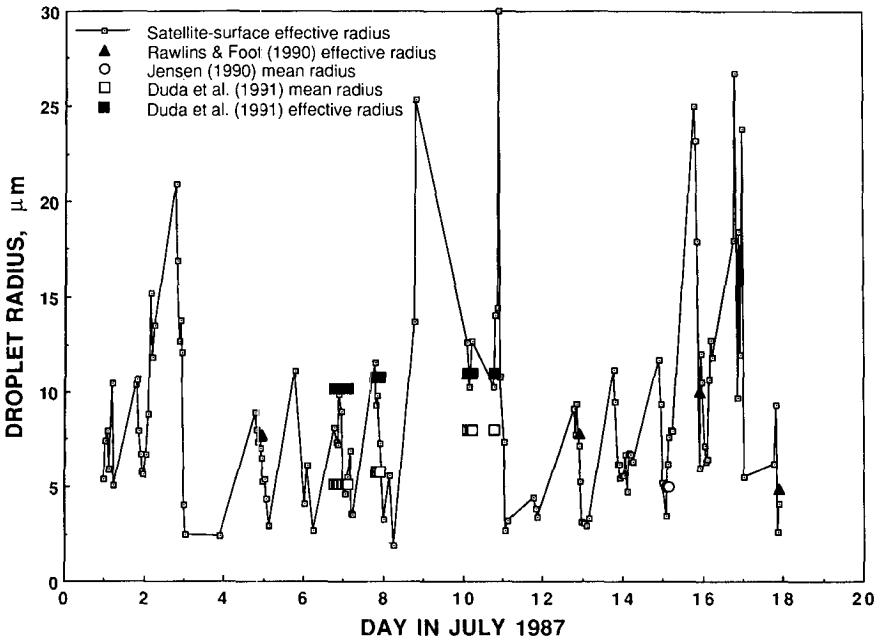

FIG. 29. Time series of effective cloud-droplet radii computed from satellite-derived region 5 cloud optical depths and SNI microwave liquid water paths. The larger symbols denote averages from in situ microphysical data taken over or within the vicinity of San Nicolas Island.

the means for a flight from 1430 to 2100 UTC. Because of time integration of the microphysical measurements and their limited spatial coverage, these comparisons do not provide a complete quantitative verification of the hourly values. They show, however, that the satellite-surface values of r are very reasonable. The effective radius inferred from optical depth is similar to the volume-effective radius and generally falls within the bounds of the microphysical data. The volume-effective radii ranged from 10 to 14 μm on 7 July, from 10 to 13 μm on 8 July, and from 10 to 13 μm during July 10–11. The respective ranges of mean droplet radius were 5–7, 5–7, and 7.5–10 μm. Overall, the cloud droplets were significantly larger during the 10 and 11 July balloon flights than during the 7 and 8 July flights. The microphysical data (Duda et al. 1989) show that the 7 and 8 July droplet-size distributions are very similar, except that some drops with radii greater than 17 μm seen during 8 July were not observed during 7 July. The mean inferred value of r is 7.2 μm on 7 July compared to 7.3 μm during 8 July. The 10 July balloon data indicate that the proportion of drops with radii greater than 7 μm is twice that observed during 7 and 8 July. During the afternoon of 10 July, there were only 3 h of satellite data that produced a mean effective radius of 11.9 μm.

The aircraft results of Jensen (1990) taken during 15 July fall between the satellite-surface–derived effective radii but are actually closest to the minimum values observed during that day. The Rawlins and Foot (1990) data were taken at a greater distance from the island and, therefore, may not be as representative of the cloud-droplet sizes within region 5 as those from the other two in situ datasets. Despite the geographical differences, the Rawlins and Foot (1990) measurements of r, which range from about 5 to 10 μm, are very consistent with the corresponding values derived from the GOES and surface microwave data.

There were no in situ data taken during the times when larger droplets ($r > 20$ μm) were inferred from the surface–satellite data. Although the values of $r > 20$ μm seen in Fig. 29 are probably unrealistic, there is some evidence that the effective radii of the droplet-size distributions were greatest at the times when these large values were retrieved. The occurrence of drizzle is a good indication of large droplets in the cloud. Droplets with radii as great as 300 μm have been observed in stratocumulus drizzle (e.g., Nicholls 1984). Drizzle over the SNI surface site was reported during the daytime on only 5 days during the IFO. Sporadic drizzle was observed during 9 July between 1200 and 2000 UTC. The last satellite observation that day, 1545 UTC, produced $r = 25$ μm. On 10 July, precipitation ended around 2200 UTC. At 2245 UTC, the first hour with satellite data, r was equal to 13 μm. The next hour, it dropped to 10 μm. The inferred values of r dropped from 30 μm at 1745 UTC 11 July to 11 μm at 1845 UTC. Drizzle ceased over SNI at about 1800 UTC that same day. Similar correspondence between the precipitation and droplet sizes was found for the other two drizzle days, 16 and 17 July. The only day in Fig. 29 with large inferred droplet sizes and no ap-

parent drizzle was 3 July. Both the LWP and the cloud albedo during the morning of 3 July were relatively low. It is not known whether drizzle was occurring in some part of the region but not over the island at this time. Drizzle may not always occur when relatively large drops are present.

Although there is general agreement between the microphysical observations and the surface-satellite retrievals, there is considerable variation in the satellite data with the effective radius ranging from 2 to 30 μm. The extreme values probably result primarily from the surface–satellite sampling mismatch discussed earlier. If the LWP observed at the surface was greater (less) than the mean LWP for region 5, the satellite would overestimate (underestimate) the effective radius of the water droplets. For example, a 20% change in LWP roughly corresponds to a 20% change in r at a given reflectance. Some variation in r is realistic as seen in the in situ data. Other error sources (scale, cloud-amount albedo errors, plane-parallel assumption, etc.) can also contribute to the variability in r.

One feature that is prevalent in the time series (Fig. 29) is the apparent diurnal variation of r. It is unclear from the microphysical data whether the apparent hourly variation in r is actually occurring or whether it is due to the various errors in the analysis. To investigate the diurnal variability, the data were averaged according to local hour and plotted in Fig. 30 with the microwave liquid water path and cloud thickness. On an hour-to-hour basis, the changes in r are not statistically significant despite the trend. The effective radii estimated during the early afternoon, however, are significantly different from the morning and late afternoon values at the 90% confidence level. Thus, it is concluded that a significant diurnal variation in effective droplet radius accompanies all the other diurnal changes in the stratocumulus clouds. Independent verification of this conclusion, however, is needed.

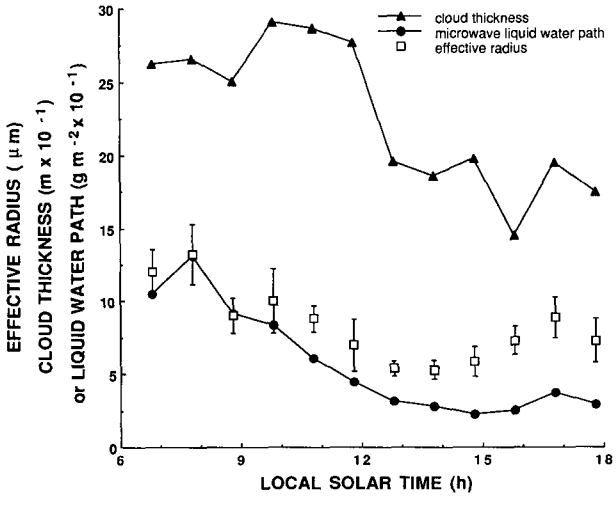

FIG. 30. Comparison of mean hourly region 5 effective cloud-droplet radius with surface-derived cloud properties over SNI, 1–19 July 1987. Error bars denote the standard error of the mean.

A complete explanation of the diurnal variation in r is beyond the scope of this paper. It is instructive, however, to consider modeling results that have examined some of the factors affecting the droplet-size distribution. For example, Bretherton (1990) used a turbulent closure model to show that drizzle can develop in a cloud-top boundary layer during the night and diminish to zero by late morning because shortwave heating decouples the cloud layer from the moisture flux. In the early morning, the LWP and droplet radius (Fig. 30) reach a maximum. These two factors should lead to drizzle, which depletes the cloud of both liquid water and large droplets, leading to a decrease in LWP and r. Except for the 10 July case, drizzle was generally observed at the surface site during the night and early morning and ended before noon, consistent with this argument. Bretherton (1990) calculated that the maximum shortwave absorption in the cloud occurs in the late morning, followed by cloud thinning and a minimum in turbulence within the cloud layer around midday. The rapid thinning of the cloud after noon (Fig. 30) and minimal turbulence are physically consistent with the decrease in the droplet radius. For a given set of conditions, droplet size depends on the time spent in growth. The diffusional growth time may be approximated by the product of the cloud depth and the vertical velocity. Thus, a droplet will spend less time growing in a thin cloud layer than in a thicker one for a constant vertical velocity. Turbulence widens the droplet distribution. The modeling results suggest, therefore, that there should be small droplets with little variation in size near noon.

Other variables such as wind speed and direction may alter the air mass, turbulence, and number and type of cloud condensation nuclei. Surface observations (Blaskovic et al. 1990) show that the mean wind direction abruptly shifts from 270° to approximately 295° at 1000 LST. The wind speed also begins to increase steadily from a minimum at 1000 LST to a maximum around 1900 LST. If this sudden wind shift results from sea-breeze effects, it would help explain both the precipitous drop in cloud thickness and the steady decrease in droplet radius. Such a shift may indicate a change in the air mass from a totally maritime origin to a mixed maritime–continental source. The number of cloud condensation nuclei would probably increase following such a change, causing a subsequent decrease in the value of r.

Potential reasons for the apparent increase in r during the late afternoon are less conspicuous. Cloud depth is nearly constant, and increased turbulence after noon is unlikely to explain all the drop size increases after 1500 LST. No significant changes are seen in the wind until 1800 LST, when it shifts to 280°. Additional meteorological data and further modeling studies would

be useful for fully explaining the variation of the droplet sizes.

This discussion indicates that the offset in the peak of the satellite-inferred and the microwave liquid water paths in Fig. 17 may be due to the use of a single effective water-droplet size in the radiative transfer model. This result implies that the optical depths derived with the 8-μm radius are in error. Figure 31 shows a comparison of the optical depths derived from the satellite data for the 8-μm radius and for the variable radius. The mean derived effective radius is 8.8 μm. On average, the fixed-radius optical depth is 0.1 less than the variable-radius value. The rms hourly difference is 0.5. Thus, only a small error is incurred by using a value of $r = 8$ μm to infer visible optical depth for this dataset.

5. Concluding remarks

The comparisons of island observations with satellite cloud-parameter retrievals have shown that the HBTM provides a reliable and relatively accurate depiction of the diurnal variations of cloud amount, height, albedo, and thickness over the region containing San Nicolas Island. The accuracy of the satellite retrievals is still somewhat elusive. Complicating factors in these analyses include the intercomparison of line and strip data with large-area measurements, a strong north–south gradient in cloud amount centered on SNI, and the effect of the island on the cloud field. Further research is needed to overcome some of the noted discrepancies. The level of agreement obtained here, despite the differences, is very encouraging for simple methods of extracting cloud parameters from operational meteorological satellite data. Because of the good agreement between the surface and the satellite cloud properties, the HBTM will be useful for verifying larger-scale results of other algorithms, such as the ISCCP, for areas containing marine stratocumulus.

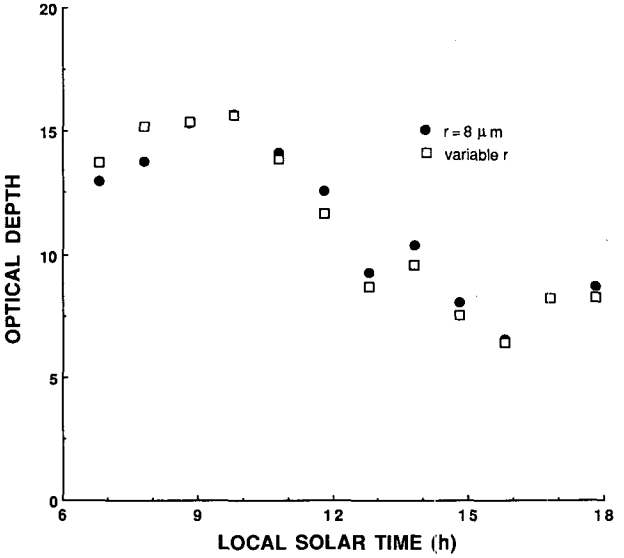

FIG. 31. Comparison of mean hourly region 5 satellite-derived optical depths using fixed ($r = 8$ μm) and variable-droplet-radius reflectance models.

The diurnal variations in cloud amount are accompanied by variations in cloud-top height, cloud thickness, cloud liquid water content, and effective droplet sizes. All of these changes must be accounted for in parameterizations of marine stratocumulus cloud processes. The variations in cloud amount and height are consistent with earlier inferences drawn from satellite observations (Minnis and Harrison 1984) about the diurnal variability of marine stratocumulus clouds and should be regarded as typical of the cloud type in the subtropics. It was also found that dissipating stratocumulus clouds can become nonblack in the infrared spectrum. The decrease in emissivity corresponds to 100 m or more in satellite-retrieved cloud-top height. Although the required height correction for emissivity is relatively small, it is significant.

Cloud thickness and cloud liquid water path are two variables that can be obtained with reasonable accuracy from the visible data. Other methods will be needed during the nighttime. The use of simultaneous liquid water and optical depth measurements to derive the effective radius of the cloud droplets was also demonstrated here. The correlative data—balloon and aircraft measurements and drizzle observations—indicate that the method provides reasonable estimates of the mean cloud-droplet sizes. Better spatial and temporal matching of the data, however, would probably produce more reliable results. The technique demonstrated here may be useful in mapping cloud-particle sizes globally from satellites equipped with collocated visible and microwave radiometers sufficient for estimating optical depth and liquid water content.

The boundary layer over San Nicolas Island is very low compared to other areas and is very near the coast, so it may be influenced by the continent. However, it provides an extreme test of both day and night satellite cloud retrievals. Although the errors determined for this region probably represent a worst case for stratocumulus, it is necessary to repeat the measurements over different regions of marine stratocumulus clouds, especially over the open ocean. Confident application of the formulas for deriving cloud liquid water path, cloud thickness, or cloud-droplet size for marine stratocumulus clouds will also require additional comparisons with ground-truth datasets. The Atlantic Stratocumulus Transition Experiment (ASTEX) in 1992 will provide a good opportunity to test these techniques and to further examine the other satellite-derived cloud properties.

Acknowledgments. The assistance of B. Joan Byars in reducing the satellite data is appreciated. The radiative transfer model was adapted from one generously

provided by K-N. Liou and Y. Takano of the University of Utah. Editorial comments by C. Thomas and W. Eberhard of the NOAA Wave Propagation Laboratory were helpful in improving the manuscript. Partial funding of the satellite analyses was provided by the Office of Naval Research under Grant USN-N0001491IMP24011.

REFERENCES

Albrecht, B. A., D. A. Randall, and S. Nicholls, 1988: Observations of marine stratocumulus clouds during FIRE. *Bull. Amer. Meteor. Soc.*, **69,** 618–626.

——, C. W. Fairall, D. W. Thomson, A. B. White, and J. B. Snider, 1990: Surface-based remote sensing of the observed and the adiabatic liquid water content of stratocumulus clouds. *Geophys. Res. Letters,* **17,** 89–92.

Blaskovic, M., R. Davies, and J. B. Snider, 1990: Diurnal variation of marine stratocumulus over San Nicolas Island during July 1987. *Mon. Wea. Rev.*, **119,** 1469–1478.

Briegleb, B. P., P. Minnis, V. Ramanathan, and E. F. Harrison, 1986: Comparison of regional clear-sky albedos inferred from the satellite observations and model computations. *J. Climate Appl. Meteor.*, **25,** 214–226.

Bretherton, C. S., 1990: Lagrangian development of a cloud-topped boundary layer in a turbulence closure model. Preprints, *Conf. Cloud Physics,* San Francisco, Amer. Meteor. Soc., 48–55.

Cox, S. K., and K. T. Griffith, 1979: Estimates of radiative divergence during Phase III of the GARP Atlantic Tropical Experiment: Part I. Methodology. *J. Atmos. Sci.*, **36,** 576–585.

Duda, D. P., G. L. Stephens, and S. K. Cox, 1989: Microphysical and radiative properties of marine stratocumulus from tethered balloon measurements. *J. Appl. Meteor.*, **30,** 170–186.

Fairall, C. W., J. E. Hare, and J. B. Snider, 1990: An eight-month sample of marine stratocumulus cloud fraction, albedo, and integrated liquid water. *J. Climate,* **3,** 847–864.

Hogg, D. C., F. O. Giraud, J. B. Snider, M. T. Decker, and E. R. Westwater, 1983: A steerable dual-channel microwave radiometer for measurement of water vapor and liquid in the atmosphere. *J. Appl. Meteor.*, **22,** 789–806.

Jensen, D. R., 1990: Horizontal variability of the marine boundary layer structure upwind of San Nicolas Island during program FIRE, 1987. *Opt. Engr.*, **29,** 127–130.

Minnis, P., and E. F. Harrison, 1984: Diurnal variability of regional cloud and clear-sky radiative parameters from GOES data. Part II: November 1978 cloud distributions. *J. Climate Appl. Meteor.*, **23,** 1012–1031.

——, ——, and G. G. Gibson, 1987: Cloud cover over the equatorial eastern Pacific derived from July 1983 International Satellite Cloud Climatology Project data using a hybrid bispectral threshold method. *J. Geophys. Res.*, **92,** 4051–4073.

Nakajima, T., and M. D. King, 1990: Determination of the optical thickness and effective particle radius of clouds from reflected solar radiation measurements. Part I: Theory. *J. Atmos. Sci.*, **47,** 1878–1893.

Nicholls, S., 1984: The dynamics of stratocumulus: Aircraft observations and comparisons with a mixed layer model. *Quart. J. Roy. Meteor. Soc.*, **110,** 783–820.

Rawlins, F., and J. S. Foot, 1990: Remotely sensed measurements of stratocumulus properties during FIRE using the C130 aircraft multichannel radiometer. *J. Atmos. Sci.*, **47,** 2488–2503.

Rossow, W. B., L. C. Garder, P. Lu, and A. Walker, 1988: International Satellite Cloud Climatology Project (ISCCP), Documentation of cloud data. *WCRP* Rep. WMO/TD-No. 266, 122pp. [Available from Dr. W. B. Rossow at NASA Goddard Space Flight Center, Institute for Space Studies, 2880 Broadway, New York, NY, 10025.]

Schiffer, R. A., and W. B. Rossow, 1983: The International Satellite Cloud Climatology Project (ISCCP): The first project of the World Climate Research Programme. *Bull. Amer. Meteor. Soc.*, **64,** 779–784.

Slingo, A., 1989: A GCM parameterization for the shortwave radiative properties of water clouds. *J. Atmos. Sci.*, **46,** 1419–1427.

Starr, D. O'C., 1987: A cirrus-cloud experiment. Intensive field observations planned for FIRE. *Bull. Amer. Meteor. Soc.*, **68,** 119–124.

Stephens, G. L., 1978: Radiation profiles in extended water clouds. *J. Atmos. Sci.*, **35,** 2123–2132.

Wiscombe, W., 1980: Improved Mie scattering algorithms. *Appl. Opt.*, **19,** 1505–1509.

Young, D. F., P. Minnis, and E. F. Harrison, 1990: Satellite-derived cloud and radiation fields over the marine stratocumulus IFO. *FIRE Science Results,* NASA CP-3079, 95–99.